Nonlinear Cascades of Surface Oceanic Geostrophic Kinetic Energy in the Frequency Domain

Nonlinear Cascades of Surface Oceanic Geostrophic Kinetic Energy in the Frequency Domain*

BRIAN K. ARBIC

Department of Earth and Environmental Sciences, University of Michigan, Ann Arbor, Michigan

ROBERT B. SCOTT

Institute for Geophysics, Jackson School of Geosciences, The University of Texas at Austin, Austin, Texas, and Department de Physique et LPO, Université de Bretagne Occidental, CNRS, Brest, France

GLENN R. FLIERL

Department of Earth, Atmospheric, and Planetary Sciences, Massachusetts Institute of Technology, Cambridge, Massachusetts

ANDREW J. MORTEN

Department of Physics, University of Michigan, Ann Arbor, Michigan

JAMES G. RICHMAN AND JAY F. SHRIVER

Oceanography Division, Naval Research Laboratory, Stennis Space Center, Mississippi

(Manuscript received 24 August 2011, in final form 31 March 2012)

ABSTRACT

Motivated by the ubiquity of time series in oceanic data, the relative lack of studies of geostrophic turbulence in the frequency domain, and the interest in quantifying the contributions of intrinsic nonlinearities to oceanic frequency spectra, this paper examines the spectra and spectral fluxes of surface oceanic geostrophic flows in the frequency domain. Spectra and spectral fluxes are computed from idealized two-layer quasigeostrophic (QG) turbulence models and realistic ocean general circulation models, as well as from gridded satellite altimeter data. The frequency spectra of the variance of streamfunction (akin to sea surface height) and of geostrophic velocity are qualitatively similar in all of these, with substantial variance extending out to low frequencies. The spectral flux $\Pi(\omega)$ of kinetic energy in the frequency ω domain for the QG model documents a tendency for nonlinearity to drive energy toward longer periods, in like manner to the inverse cascade toward larger length scales documented in calculations of the spectral flux $\Pi(k)$ in the wavenumber k domain. Computations of $\Pi(\omega)$ in the realistic model also display an ''inverse temporal cascade.'' In satellite altimeter data, some regions are dominated by an inverse temporal cascade, whereas others exhibit a forward temporal cascade. However, calculations performed with temporally and/or spatially filtered output from the models demonstrate that $\Pi(\omega)$ values are highly susceptible to the smoothing inherent in the construction of gridded altimeter products. Therefore, at present it is difficult to say whether the forward temporal cascades seen in some regions in altimeter data represent physics that is missing in the models studied here or merely sampling artifacts.

1. Introduction

In this paper, we examine the spectra and spectral fluxes of surface oceanic geostrophic flows in the frequency domain. We will calculate spectra and spectral fluxes from the outputs of a highly simplified (idealized) two-layer quasigeostrophic (QG) turbulence model (Arbic and Flierl 2004) and a high-resolution ocean general circulation model run in a realistic near-global

* Naval Research Laboratory Contribution Number NRL/JA/7320-2011-803, and The University of Texas at Austin Institute for Geophysics Contribution Number 2471.

Corresponding author address: Dr. Brian K. Arbic, Department of Earth and Environmental Sciences, University of Michigan, Ann Arbor, MI 48109-1005.
E-mail: arbic@umich.edu

DOI: 10.1175/JPO-D-11-0151.1

domain (called here, the realistic model; Hurlburt and Thompson 1980; Shriver et al. 2007), as well as from gridded satellite altimeter data (LeTraon et al. 1998; Ducet et al. 2000). We are motivated in part by the fact that oceanic data is often in the frequency domain (taking a current meter as an example). However, as noted by Ferrari and Wunsch (2010), geostrophic turbulence remains much better theoretically developed in the wavenumber domain (taking the substantial literature on spectral slopes in wavenumber space as an example; e.g. Vallis 2006). As far as we know, this paper represents the first comprehensive look at idealized QG turbulence in the frequency domain. We will describe spectra and spectral slopes computed from idealized QG models and compare the results to those from realistic ocean models and oceanic datasets. Finally, another primary motivation for this study is the interest in quantifying the contributions of intrinsic nonlinearities in oceanic dynamics to oceanic frequency spectra. As described below, we will quantify nonlinear contributions through computations of spectral fluxes. Some important related issues discussed in the paper include the Taylor (1938) hypothesis relating frequency and wavenumber spectra, the sensitivity of QG turbulence statistics in the frequency domain to bottom friction, and the impact of the spatial and temporal filtering inherent in the creation of gridded satellite altimeter data on the computed spectral fluxes.

We will adapt some of the language and results of geostrophic turbulence theory, which is generally associated with the wavenumber domain, to the frequency domain. For instance, we will build an analog in the frequency domain for the diagnosis of the inverse cascade to larger spatial scales commonly done in the wavenumber domain. Recently, the spectral fluxes $\Pi(k)$ of kinetic energy in wavenumber k space for surface ocean geostrophic flows have been computed from satellite altimetry data of sea surface height (Scott and Wang 2005).[1] Following upon this, $\Pi(k)$ has been computed from both idealized QG turbulence models (e.g., Scott and Arbic 2007) and realistic ocean general circulation models (e.g., Schlösser and Eden 2007) (see also Tulloch et al. 2011). All three types of computations demonstrate that there is an inverse cascade of kinetic energy, driven by nonlinear advection, toward larger spatial scales taking place at length scales sufficiently large [when compared to the first baroclinic (BC) mode deformation radius L_d]. Motivated by these studies, here we investigate spectral fluxes $\Pi(\omega)$ and spectral transfers

$$T(\omega) = -\frac{\partial}{\partial \omega}\Pi(\omega)$$

of kinetic energy in frequency ω space, as diagnostics of the impact of nonlinearity on the frequency spectra of surface ocean geostrophic flows. Our analysis of nonlinearities in the frequency domain is somewhat similar to the diagnostics employed by Sheng and Hayashi (1990a,b) on realistic atmospheric models and atmospheric datasets. Note that our focus is on geostrophic flows, computed from derivatives of sea surface height (more precisely streamfunction) via the geostrophic relations.

In analogy to the spectral fluxes in wavenumber space, we might expect that, at low frequencies, the spectral fluxes in frequency space will exhibit cascades toward yet lower frequencies (longer time scales). Indeed, the Taylor hypothesis (Taylor 1938) suggests that under certain conditions (e.g., turbulent velocities u' that are small compared to a mean flow velocity U) the wavenumber and frequency domains are related simply, via the formula $\omega = Uk$. In this case, spectra in wavenumber and frequency space would have the same slopes, and phenomena in the wavenumber domain (e.g., the inverse cascade) should have analogs in frequency space. Further motivation arises from analysis of realistic atmospheric models and atmospheric datasets in the frequency domain, which demonstrate an energy transfer from high-frequency motions to low-frequency motions in the extratropics (Sheng and Hayashi 1990a,b), and from experiments on acoustic turbulence in superfluid helium, in which an inverse energy cascade in frequency space takes place under certain conditions (Ganshin et al. 2008; Efimov et al. 2009, 2010).

Substantial variance often extends out to the lowest frequencies in geophysical records, set by the duration of the record (e.g., Richman et al. 1977; Wunsch 2009, 2010, and references therein), and there is great interest in examining potential causes of this low-frequency variability. An ultimate goal of the work begun here is to understand the degree to which oceanic frequency spectra in the geostrophic regime (as measured by, e.g., current meters or satellite altimetry) are caused by intrinsic nonlinearities in the oceanic dynamics (a process emphasized in this paper) as opposed to, for instance, the oceanic response to atmospheric wind forcing (e.g., Hasselmann 1976).

Another topic we will explore in this paper is the sensitivity of eddy statistics in frequency space to the strength of linear bottom Ekman friction. Several recent

[1] In this paper, k denotes isotropic wavenumber except where noted; in a few places in section 2, k and l denote wavenumbers in the x and y directions, respectively.

papers have demonstrated that the length scales and other statistics in stratified geostrophic turbulence are highly sensitive to the strength of linear bottom Ekman friction (Arbic and Flierl 2003, 2004; Riviere et al. 2004; Thompson and Young 2006, 2007; Arbic et al. 2007). Arbic and Scott (2008) showed that a qualitatively similar sensitivity holds when the bottom friction is quadratic. Motivated by these results, here we briefly examine the sensitivity of statistics computed in the frequency domain to linear bottom Ekman friction.

We will also examine the impact of filtering a geostrophic streamfunction in space and time on the estimated spectral fluxes. This topic is important because the Archiving, Validation, and Interpretation of Satellite Oceanographic data (AVISO) gridded satellite altimeter products (Le Traon et al. 1998; Ducet et al. 2000) used here to compute spectral kinetic energy fluxes are constructed by interpolating along-track data from two altimeters, in space and time, onto a 1/3° Mercator grid. The Ocean Topography Experiment (TOPEX)/Poseidon and *Jason-1* altimeter data utilized in this construction have high along-track resolution (about 6 km) but a large distance between adjacent tracks (about 300 km; Chelton et al. 2001). Because of the large along-track distance, the actual feature resolution of AVISO data is much coarser than 6 km (Chelton et al. 2011). The interpolation procedure used to construct the gridded AVISO data acts as a smoother of the raw along-track data, in both space and time. We will examine the impact of such smoothing on spectral flux estimates by comparing fluxes computed from unfiltered versus filtered outputs of the idealized QG models and realistic ocean models.

We will examine the consistency of slopes of streamfunction and geostrophic velocity variance in the frequency domain between idealized QG models, realistic ocean models, and gridded satellite altimeter data. The slopes of spectra in frequency and wavenumber space are of great practical and theoretical interest. The advent of satellite altimetry has made it possible to compute spectral slopes on global scales and to compare the results with theoretical predictions. See, for instance, Le Traon et al. (2008) and Xu and Fu (2011), who compute wavenumber spectra, and Hughes and Williams (2010) and Wunsch (2009, 2010), who compute frequency spectra. See also Hayashi and Golder (1977) and Hayashi (1982), who discuss the space–time spectra of realistic atmospheric models and datasets. As noted, if the Taylor hypothesis holds, the slopes in frequency and wavenumber space will be identical. Therefore, if the Taylor hypothesis holds, the slopes of streamfunction and geostrophic velocity variance spectra in frequency space will differ by -2, as in wavenumber space (because geostrophic velocity is the derivative of streamfunction and a spatial derivative in physical space is equivalent to multiplication by k in wavenumber space). However, there are other considerations, such as Kolmogorov-like arguments that predict a -2 slope for an energy cascade in frequency space versus $-5/3$ in wavenumber space (Tennekes and Lumley 1972).

The paper is organized as follows: In section 2, we present results from the QG turbulence model. After discussing the model limitations and governing equations and displaying some typical flow fields, we display frequency spectra and the sensitivity of the QG results in frequency space to the strength of bottom Ekman friction. We then describe the theory behind spectral fluxes of kinetic energy in frequency space and demonstrate the critical role that the spectral kinetic energy flux term plays in an ''integral energy budget.'' Next, we demonstrate the necessity for averaging over many grid points in order to estimate spectral fluxes in frequency space. Following that, we demonstrate the dependence of estimates of spectra and spectral fluxes in frequency space on the duration and sampling frequency of the time series involved. Section 2 concludes with a discussion of the substantial impact that filtering in space or time can have on spectral flux estimates made from the QG model. In sections 3 and 4, we present spectra and spectral fluxes in frequency space, computed from the realistic high-resolution numerical ocean general circulation model and from gridded satellite altimeter data, respectively. To complement the filtering exercise done with the QG model and to further aid in interpreting the altimeter results, section 3 also presents spectral fluxes computed from temporally smoothed versions of the realistic model output. A summary and discussion is given in section 5.

2. Results from idealized quasigeostrophic model

a. Model description, governing equations, and example flow fields

Our two-layer QG turbulence model is highly simplified. There is no planetary beta effect or bottom topography, and there are only two vertical modes [barotropic (BT) and first mode baroclinic]. The lack of planetary beta excludes Rossby waves (e.g., Pedlosky 1987; Vallis 2006), which are an important component of surface oceanic variability (see, e.g., Fig. 5 in Wunsch 2010). Nevertheless, we will see that the frequency spectra and spectral fluxes in the idealized QG model compare well qualitatively with those in our realistic ocean model.

The QG model is forced by an imposed mean flow, which is horizontally homogeneous within each layer but

vertically sheared between the layers and is therefore baroclinically unstable on the f plane, which we assume here for simplicity. The imposed mean flow may be thought of as representing the time-mean gyre flow in a large patch of the ocean. The model is doubly periodic and has 256 grid points on a side (thus 256^2 grid points in all), where each side has dimensional length $20\pi L_d$. The model is initialized with a randomly generated initial condition and achieves statistical equilibrium when the energy extracted by eddies from the mean flow is balanced by energy dissipation.

As in our earlier papers on QG turbulence, the governing equations of the model are written as in Flierl (1978). The Flierl (1978) equations, which can be written in either modal or layer form, bring out the two dynamically significant properties of the system–the decay scale as embodied in a single internal deformation radius and the baroclinic self-interaction term. In layer form, the governing equations are

$$\frac{\partial q_1}{\partial t} + \Gamma_1 + J(\psi_1, q_1) = \text{ssd} \quad \text{and} \tag{1}$$

$$\frac{\partial q_2}{\partial t} + \Gamma_2 + J(\psi_2, q_2) = -R_2\nabla^2\psi_2 + \text{ssd}, \tag{2}$$

where t is time; potential vorticity q is the prognostic variable; ssd indicates small-scale dissipation; and the subscripts 1 and 2 denote the upper and lower layers, respectively. The perturbation streamfunctions ψ_1 and ψ_2 satisfy

$$q_1 = \nabla^2\psi_1 + \frac{(\psi_2 - \psi_1)}{(1+\delta)L_d^2}, \quad q_2 = \nabla^2\psi_2 + \frac{\delta(\psi_1 - \psi_2)}{(1+\delta)L_d^2}, \tag{3}$$

where $\delta = H_1/H_2$, the ratio of upper- to lower-layer depths, and the first baroclinic mode deformation radius L_d is defined as in Flierl (1978) to be $[g'H_1H_2/f_0^2(H_1+H_2)]^{1/2}$, where g' is reduced gravity and f_0 is the Coriolis parameter (e.g., Vallis 2006).[2] The upper-layer streamfunction is the quantity in the QG model that is most closely analogous to sea surface height. The zonal (east–west) and meridional (north–south) coordinates are x and y, respectively, and $J(A, B) = \partial A/\partial x\, \partial B/\partial y - \partial A/\partial y\, \partial B/\partial x$. The forcing terms are

$$\Gamma_1 = \overline{u_1}\frac{\partial q_1}{\partial x} + \frac{\partial \overline{q_1}}{\partial y}\frac{\partial \psi_1}{\partial x} \quad \text{and} \tag{4}$$

$$\Gamma_2 = \overline{u_2}\frac{\partial q_2}{\partial x} + \frac{\partial \overline{q_2}}{\partial y}\frac{\partial \psi_2}{\partial x}, \tag{5}$$

where fluctuations from the mean are written without overbars, whereas imposed time-mean quantities are designated with overbars. The zonal velocity is u, the meridional velocity is v, and the imposed mean flow is taken to be zonal. The imposed mean PV gradients are

$$\frac{\partial \overline{q_1}}{\partial y} = \frac{(\overline{u_1} - \overline{u_2})}{(1+\delta)L_d^2}, \quad \frac{\partial \overline{q_2}}{\partial y} = \frac{\delta(\overline{u_2} - \overline{u_1})}{(1+\delta)L_d^2}. \tag{6}$$

The bottom boundary layer thickness $d_{\text{Ekman}} = \sqrt{A/f_0}$ determines the bottom Ekman drag R_2 by

$$R_2 = \frac{f_0 d_{\text{Ekman}}}{2H_2}, \tag{7}$$

where A is the vertical eddy viscosity.

The ssd used here is an exponential cutoff filter in wavenumber space (Canuto et al. 1988; LaCasce 1996),

$$\text{filter} = \exp\left[-\alpha\left(\sqrt{k^2+l^2} - k_0\right)^M\right] \quad \text{when} \quad \sqrt{k^2+l^2} > k_0,$$
$$\text{filter} = 1.0 \quad \text{when} \quad \sqrt{k^2+l^2} \le k_0, \tag{8}$$

where k and l are wavenumbers in the x and y directions, respectively, and k_0 is the cutoff wavenumber. We take $\alpha = 18.4$, $M = 4$, and $k_0 = 0.65k_N$, where k_N corresponds to the Nyquist scale. The filter is applied to $\hat{q_1}$ and $\hat{q_2}$, the Fourier transforms of q_1 and q_2, at every time step. As shown by LaCasce (1996), the wavenumber filter does not distort modons (Stern 1975, Larichev and Reznik 1976a,b), which are exact solutions of the inviscid nonlinear QG equations, nearly as much as eddy viscosities or hyperviscosities do. This suggests that the wavenumber filter is a very "clean" choice for small-scale dissipation. A disadvantage of the filter is that it is not simple to diagnose its impact on the energy and enstrophy budgets, because it acts on $\hat{q}$ instead of $d\hat{q}/dt$. We infer its impact as a residual of the other terms in the budget.

BT and BC modes are defined as in Flierl (1978),

$$\psi_{\text{BT}} = \frac{\delta\psi_1 + \psi_2}{1+\delta}, \quad \psi_{\text{BC}} = \frac{\sqrt{\delta}(\psi_1 - \psi_2)}{1+\delta},$$
$$q_{\text{BT}} = \frac{\delta q_1 + q_2}{1+\delta} = \nabla^2\psi_{\text{BT}},$$
$$q_{\text{BC}} = \frac{\sqrt{\delta}(q_1 - q_2)}{1+\delta} = \nabla^2\psi_{\text{BC}} - \frac{1}{L_d^2}\psi_{\text{BC}}. \tag{9}$$

[2] Note that in Vallis (2006) the two-layer QG model is defined to have a single deformation radius as is the case here. Some treatments of the QG equations differ slightly. For instance, in Pedlosky (1987), the two-layer QG model contains two distinct internal deformation radii.

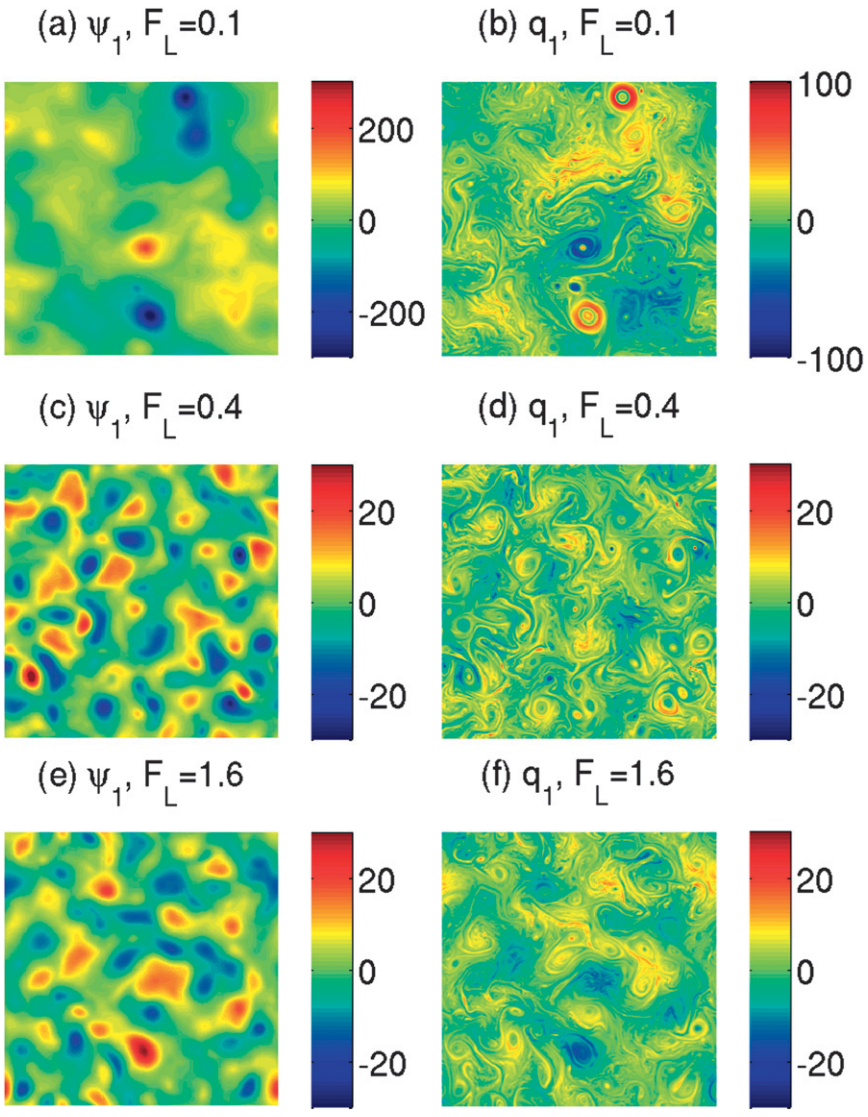

FIG. 1. Snapshots of (left) upper-layer streamfunction ψ_1 and (right) upper-layer potential vorticity q_1 for idealized two-layer QG simulations with nondimensional bottom friction values (top)–(bottom) $F_L = 0.1$, 0.4, and 1.6.

The QG equations above are governed by two nondimensional parameters. In the runs performed here, δ is set to 0.2, a value that yields a strength of the first baroclinic mode self-interaction in the two-layer model consistent with that obtained from typical midlatitude stratification profiles (Flierl 1978; Fu and Flierl 1980). The nondimensional linear bottom Ekman friction strength $F_L = R_2 L_d/(\overline{u}_1 - \overline{u}_2)$ is set to 0.4 in the "nominal" run presented here, which we will focus most of our efforts on. This F_L value yields amplitudes, horizontal scales, and vertical structure of eddy kinetic energy that agree reasonably well with midlatitude observations (Arbic and Flierl 2004).

Figure 1 displays snapshots of ψ_1 and q_1 for F_L values of 0.1 and 1.6 as well as the nominal value of 0.4. The $F_L = 0.4$ flow field consists of densely packed weak vortices, not unlike a typical snapshot of sea surface height in the midocean (see, e.g., comparisons of model and observations in Fig. 10 of Arbic and Flierl 2004). In the $F_L = 0.1$ (weaker friction) experiment, isolated coherent vortices (e.g., McWilliams 1984) dominate the ψ_1 and especially q_1 fields.

b. *Frequency spectra of idealized model*

As is standard, the model output is windowed, so that the beginning and ending of the time series taper toward

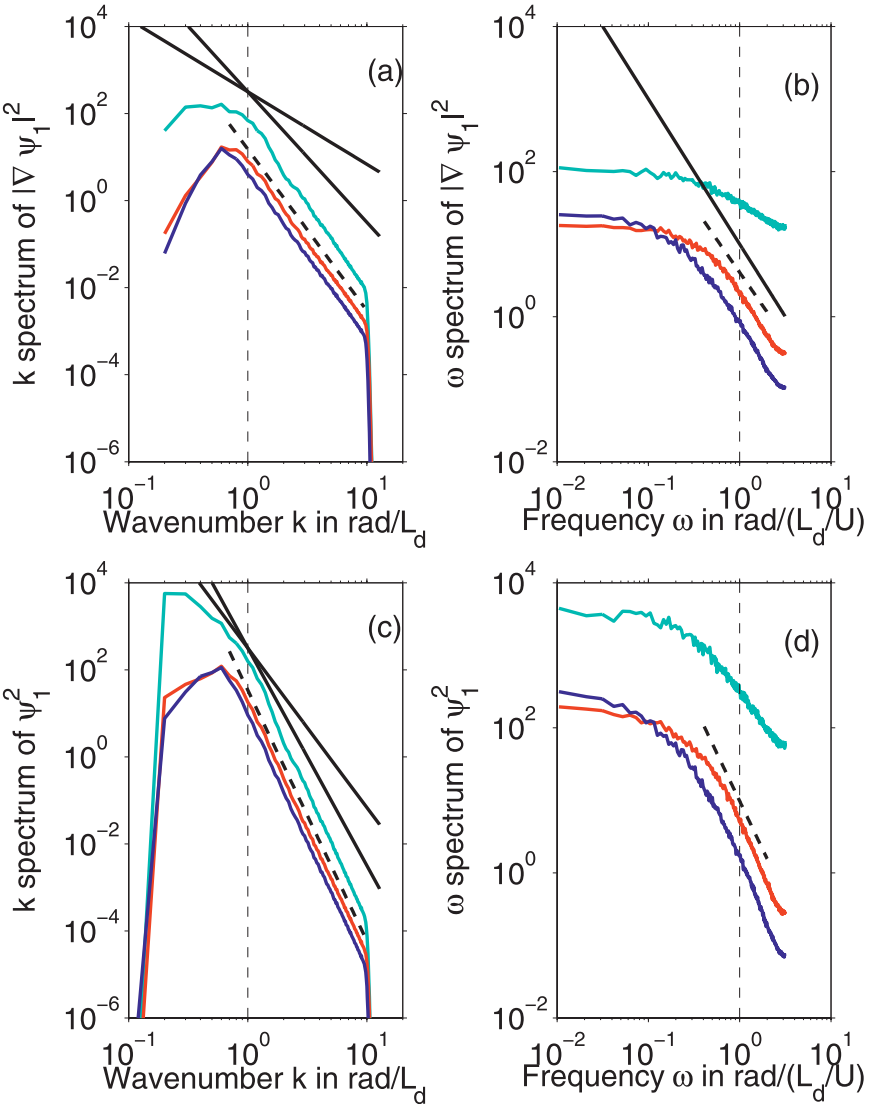

FIG. 2. (a) Wavenumber k spectrum of upper-layer kinetic energy $|\nabla\psi_1|^2$ in two-layer QG turbulence model. (b) Frequency ω spectrum of $|\nabla\psi_1|^2$. (c) Wavenumber spectrum of upper-layer streamfunction variance ψ_1^2. (d) Frequency spectrum of ψ_1^2. Cyan, red, and blue curves denote experiments with nondimensional bottom friction values $F_L = 0.1$, 0.4, and 1.6, respectively. Thick solid black lines have been included to show slopes of (a) $-5/3$ and -3, (b) -2, and (c) $-11/3$ and -5. Thick dashed black lines in (a)–(d) are least squares fits to the red curve over the range of wavenumbers or frequencies covered by the lines, with slopes of -3.7, -1.8, -5.8, and -2.6, respectively; y values in dashed black lines are multiplied by 2 for clarity. In this and other plots of QG results, U in the x-axis label denotes $\overline{u}_1 - \overline{u}_2$.

zero, before Fourier transforms are computed in frequency space. We utilize nine overlapping Hanning windows, each having width equal to one-fifth of the total time interval. Other windows were tried and found to yield similar results.

The wavenumber and frequency spectra of the upper-layer streamfunction variance ψ_1^2 and of the upper-layer kinetic energy $|\nabla\psi_1|^2$ are displayed in Fig. 2. The computations in Fig. 2 are done with 600 snapshots, where each snapshot is one unit of nondimensional time $L_d/(\overline{u}_1 - \overline{u}_2)$ apart. The correlation time (as measured by the zero crossing in the autocorrelation) is about 16.5 snapshots for the $F_L = 0.4$ run and a similar number for the other runs shown in Fig. 2.

Results in Fig. 2 are displayed from the nominal run with $F_L = 0.4$, as well as from runs with F_L equal to 0.1

and 1.6. As discussed in Arbic and Flierl (2004) and other sources (e.g., Thompson and Young 2006, 2007), as the friction strength decreases (F_L decreases), the inverse cascade reaches out to larger scales, such that the wavenumber spectrum reddens (cyan curves in Figs. 2a,c). Figure 2a, the wavenumber spectrum plot of kinetic energy, displays the canonical slope values of $-5/3$ and -3, representing the classical predictions in energy and enstrophy cascade regimes (Vallis 2006), as thick solid black lines. Figure 2c, the wavenumber spectrum plot of streamfunction variance, displays the classical slope values of $-11/3$ and -5, obtained from the $-5/3$ and -3 slopes through division by k^2. At the high-wavenumber end but before the sharp dropoff due to the action of the wavenumber filter, the slopes of the streamfunction variance and kinetic energy in the $F_L = 0.4$ run are -5.8 and -3.7, respectively, as determined from least squares fits over the range indicated by the thick dashed black lines. These slopes differ (to within "estimation errors") by -2, as anticipated, and are somewhat steeper than the -5 and -3 predictions from the enstrophy cascade.

The frequency spectra of the model (Figs. 2b,d) display a steeper slope at higher frequencies and a flatter slope at lower frequencies. This basic shape is also found in frequency spectra computed from current-meter records (e.g., Richman et al. 1977; Ferrari and Wunsch 2010; and references therein) and in frequency spectra computed in previous studies using altimeter data (e.g., Wunsch 2009, 2010, and references therein). In contrast to the wavenumber spectra, which turn over at low wavenumbers, the frequency spectra continue to be energetic (stay flat) at the lowest frequencies. In Fig. 2b, the thick solid line is at a slope of -2, the predicted slope for an energy cascade in the frequency domain (Tennekes and Lumley 1972). In Figs. 2b,d, the thick dashed lines represent least squares fits to the frequency spectra of velocity and streamfunction variance, respectively, over the windows covered by the lines, from the $F_L = 0.4$ run. The slopes over these windows are -1.8 and -2.6 for velocity and streamfunction variance, respectively. The velocity variance slope is close to the predicted -2 slope, as are slopes computed from current-meter-derived frequency spectra (e.g., Richman et al. 1977; Ferrari and Wunsch 2010; and references therein). The model slopes of -1.8 and -2.6 are not equal to what is seen at the high-wavenumber end in the wavenumber spectrum, and they do not differ by -2, as do the slopes of these quantities in wavenumber space. The Taylor (1938) hypothesis relating wavenumber to frequency spectra thus fails quantitatively in both respects. At the low-frequency end, the slopes of upper-layer streamfunction and velocity variance are -0.4 and -0.1, respectively, as determined from least squares fits over a decade of frequencies. These slopes also do not differ by -2.

c. *Sensitivity of time scales in idealized model to Ekman friction*

In this section, we compare the sensitivity of eddy time scales to linear bottom Ekman friction with the previously documented sensitivity of eddy length scales to bottom Ekman friction. As is common (e.g., Vallis 2006), we define length scales $\mathcal{L}$ as reciprocals of the first moment (centroid) of the wavenumber spectrum $E(k)$. For instance, the length scale $\mathcal{L}_{\rm BT}$ of the barotropic mode is

$$\mathcal{L}_{\rm BT} = \left(\frac{\int k E_{\rm BT}(k)\, dk}{\int E_{\rm BT}(k)\, dk} \right)^{-1}, \tag{10}$$

where $E_{\rm BT}(k)$ is the wavenumber spectrum of barotropic kinetic energy. Likewise, we define model time scales $\mathcal{T}$ as reciprocals of the centroid of the frequency spectrum $E(\omega)$ in question. For instance,

$$\mathcal{T}_{\rm BT} = \left(\frac{\int \omega E_{\rm BT}(\omega)\, d\omega}{\int E_{\rm BT}(\omega)\, d\omega} \right)^{-1}, \tag{11}$$

where $E_{\rm BT}(\omega)$ is the frequency spectrum of barotropic kinetic energy. For these quantities to be well defined, the wavenumber and frequency spectral slopes must fall off more steeply than -2 at the high-wavenumber and high-frequency ends and less steeply than -1 at the low-wavenumber and low-frequency ends. The nominal $F_L = 0.4$ simulation satisfies these constraints, with the exception of the kinetic energy at high frequencies, which falls off as -1.8. As will be discussed later, a simulation of the nominal QG solution with higher sampling frequency shows slopes steeper than -2 at the high-frequency end, which thus satisfies the constraints for ω_E to be well defined. The values of ω_E computed from the two cases are nearly identical.

The length and time scales of the barotropic mode, baroclinic mode, and upper layer, in QG simulations with different bottom friction values, are displayed in Fig. 3. Length scales $\mathcal{L}$ (dashed curves with squares) are normalized by L_d while time scales $\mathcal{T}$ (solid curves with x's) are normalized by $L_d/(\overline{u}_1 - \overline{u}_2)$. In the weak friction regime (F_L of order one or less), as friction further weakens the length scales of the barotropic mode and upper layer increase, whereas the baroclinic length scale remains relatively constant. In the weak friction regime, the kinetic energies associated with each mode or layer increase more rapidly with further decreases in friction

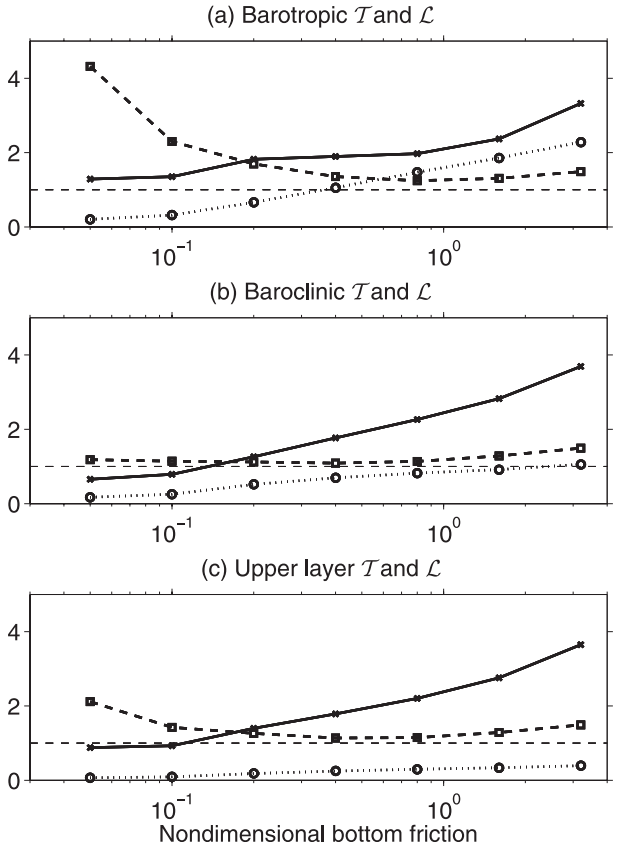

FIG. 3. Length scales $\mathcal{L}$ and time scales $\mathcal{T}$ of the kinetic energy in the (a) barotropic mode, (b) baroclinic mode, and (c) upper layer, in two-layer QG turbulence experiments damped by bottom friction, as a function of nondimensional bottom friction strength. Length (time) scales are computed as the reciprocal of the first moment of the appropriate wavenumber (frequency) spectrum. Length scales are given by dashed curves with squares and are normalized by L_d, whereas time scales are given by solid curves with x's and are normalized by $L_d/(\overline{u}_1 - \overline{u}_2)$. Dotted curves with circles are the predicted time scales obtained by dividing the length scale $\mathcal{L}$ by the rms velocity scale associated with the layer or mode in question. Dashed horizontal lines are drawn at the value of 1.

than the length scales do (see, e.g., Figs. 4–6 of Arbic and Flierl 2004). Therefore, if we crudely estimate the time scale by $\mathcal{T} = \mathcal{L}/U_{\rm rms}$, where $U_{\rm rms}$ is the rms velocity of the mode or layer in question, then we might expect a decrease in $\mathcal{T}$ with decreasing friction. Figure 3 demonstrates that these predicted time scales (dotted curves with circles) do indeed decrease with decreasing friction strength. The actual time scales computed from (11) also decrease with decreasing friction. Thus, the trend of the changes in time scale with changes in friction is successfully predicted by the above argument. However, the actual time scales are larger than the predicted time scales. The actual barotropic time scale exceeds $L_d/(\overline{u_1} - \overline{u_2})$ in all of the experiments analyzed here. In most of these experiments, the time scale exceeds this value for the upper layer and baroclinic modes, as well as for the barotropic mode. This tendency for time scales to exceed $L_d/(\overline{u_1} - \overline{u_2})$ mimics the tendency for length scales to exceed L_d, although the tendency is not as rigid in the case of the time scales. Some of the time scales drop below the dashed lines set at unity in Fig. 3, whereas the length scales never drop below these lines.

d. Theory of spectral fluxes in frequency space

To develop the theory of $\Pi(\omega)$, we let

$$\psi_1(x,y,t) = \sum_k \sum_l \sum_\omega \widehat{\psi_1}(k,l,\omega) e^{i(kx+ly+\omega t)},$$
$$\psi_2(x,y,t) = \sum_k \sum_l \sum_\omega \widehat{\psi_2}(k,l,\omega) e^{i(kx+ly+\omega t)}, \quad (12)$$

where $\widehat{\psi}$ denotes a Fourier transform of ψ in wavenumber–frequency space and k and l are zonal and meridional wavenumbers, respectively. If we neglect the small-scale dissipation, the Fourier transformed upper- and lower-layer governing equations are

$$-i\omega\left(K^2 + \frac{1}{(1+\delta)L_d^2}\right)\widehat{\psi_1}(k,l,\omega) + i\omega\frac{1}{(1+\delta)L_d^2}\widehat{\psi_2}(k,l,\omega) + \widehat{J(\psi_1,\nabla^2\psi_1)}(k,l,\omega) + \frac{1}{(1+\delta)L_d^2}\widehat{J(\psi_1,\psi_2)}(k,l,\omega) + \widehat{\Gamma_1}(k,l,\omega) = 0 \quad (13)$$

and

$$-i\omega\left(K^2 + \frac{\delta}{(1+\delta)L_d^2}\right)\widehat{\psi_2}(k,l,\omega) + i\omega\frac{\delta}{(1+\delta)L_d^2}\widehat{\psi_1}(k,l,\omega) + \widehat{J(\psi_2,\nabla^2\psi_2)}(k,l,\omega) + \frac{\delta}{(1+\delta)L_d^2}\widehat{J(\psi_2,\psi_1)}(k,l,\omega) + \widehat{\Gamma_2}(k,l,\omega) = R_2K^2\widehat{\psi_2}(k,l,\omega), \quad (14)$$

respectively, where $K^2 = k^2 + l^2$ and we have dropped the summation signs for simplicity.

To obtain the depth-averaged energy equation, we multiply (13) by $-(\delta/1+\delta)\widehat{\psi_1}^*(k,l,\omega)$, where the superscript asterisk represents a complex conjugate, and the complex conjugate of (13) by $-(\delta/1+\delta)\widehat{\psi_1}(k,l,\omega)$; add the results; and divide by 2. Similarly, we multiply (14) by $-(1/1+\delta)\widehat{\psi_2}^*(k,l,\omega)$ and the complex conjugate of (14) by $-(1/1+\delta)\widehat{\psi_2}(k,l,\omega)$, add the results, and divide by 2. We then add everything together and find that the terms involving $i\omega$ in (13) and (14) drop out. Utilizing the identity $(a^*b + ab^*)/2 = \mathrm{Re}[a^*b]$, where Re denotes the real part of a complex number, we are left with

$$\mathrm{Re}\left[\frac{\delta}{1+\delta}\widehat{\psi_1}^*(k,l,\omega)\widehat{J(\psi_1,\nabla^2\psi_1)}(k,l,\omega)\right]+\mathrm{Re}\left[\frac{1}{1+\delta}\widehat{\psi_2}^*(k,l,\omega)\widehat{J(\psi_2,\nabla^2\psi_2)}(k,l,\omega)\right]$$
$$+\mathrm{Re}\left[\frac{\delta}{(1+\delta)^2L_d^2}\widehat{(\psi_1-\psi_2)}^*(k,l,\omega)\widehat{J(\psi_1,\psi_2)}(k,l,\omega)\right]+\mathrm{Re}\left[\frac{\delta}{1+\delta}\widehat{\psi_1}^*(k,l,\omega)\widehat{\Gamma_1}(k,l,\omega)\right]$$
$$+\mathrm{Re}\left[\frac{1}{1+\delta}\widehat{\psi_2}^*(k,l,\omega)\widehat{\Gamma_2}(k,l,\omega)\right]-\frac{1}{1+\delta}R_2K^2\widehat{\psi_2}^*(k,l,\omega)\widehat{\psi_2}(k,l,\omega)=0. \quad (15)$$

To simplify the interpretation of (15), we utilize the following definitions: The spectral transfers of upper- and lower-layer kinetic energy are

$$T_{\mathrm{KE},1}(k,l,\omega)=\mathrm{Re}\left[\frac{\delta}{1+\delta}\widehat{\psi_1}^*(k,l,\omega)\widehat{J(\psi_1,\nabla^2\psi_1)}(k,l,\omega)\right]$$

and (16)

$$T_{\mathrm{KE},2}(k,l,\omega)=\mathrm{Re}\left[\frac{1}{1+\delta}\widehat{\psi_2}^*(k,l,\omega)\widehat{J(\psi_2,\nabla^2\psi_2)}(k,l,\omega)\right], \quad (17)$$

respectively. The spectral transfer of available potential energy (APE) is

$$T_{\mathrm{APE}}(k,l,\omega)=\mathrm{Re}\left[\frac{\delta}{(1+\delta)^2L_d^2}\widehat{(\psi_1-\psi_2)}^*(k,l,\omega)\widehat{J(\psi_1,\psi_2)}(k,l,\omega)\right]. \quad (18)$$

The spectral transfer due to the imposed mean flow forcing is

$$T_{\mathrm{forcing}}(k,l,\omega)=\mathrm{Re}\left[\frac{\delta}{1+\delta}\widehat{\psi_1}^*(k,l,\omega)\widehat{\Gamma_1}(k,l,\omega)+\frac{1}{1+\delta}\widehat{\psi_2}^*(k,l,\omega)\widehat{\Gamma_2}(k,l,\omega)\right], \quad (19)$$

and the spectral transfer due to bottom Ekman friction is

$$T_{\mathrm{friction}}(k,l,\omega)=-\frac{1}{1+\delta}R_2K^2\widehat{\psi_2}^*(k,l,\omega)\widehat{\psi_2}(k,l,\omega). \quad (20)$$

With these definitions, (15) becomes

$$T_{\mathrm{KE},1}(k,l,\omega)+T_{\mathrm{KE},2}(k,l,\omega)+T_{\mathrm{APE}}(k,l,\omega)+T_{\mathrm{forcing}}(k,l,\omega)+T_{\mathrm{friction}}(k,l,\omega)=0. \quad (21)$$

Spectral fluxes are defined by integrating the spectral transfers over some part of (k, l, ω) space. For instance, integration over all values of ω and over a semi-infinite range of wavenumbers yields spectral fluxes in wavenumber space,

$$\Pi_{\mathrm{KE},1}(K)=\int_{k^2+l^2\geq K^2}\int\int T_{\mathrm{KE},1}(k,l,\omega)\,d\omega\,dk\,dl, \quad (22)$$

$$\Pi_{\mathrm{KE},2}(K)=\int_{k^2+l^2\geq K^2}\int\int T_{\mathrm{KE},2}(k,l,\omega)\,d\omega\,dk\,dl, \quad (23)$$

$$\Pi_{\mathrm{APE}}(K)=\int_{k^2+l^2\geq K^2}\int\int T_{\mathrm{APE}}(k,l,\omega)\,d\omega\,dk\,dl, \quad (24)$$

$$\Pi_{\mathrm{forcing}}(K)=\int_{k^2+l^2\geq K^2}\int\int T_{\mathrm{forcing}}(k,l,\omega)\,d\omega\,dk\,dl, \quad \text{and} \quad (25)$$

$$\Pi_{\mathrm{friction}}(K)=\int_{k^2+l^2\geq K^2}\int\int T_{\mathrm{friction}}(k,l,\omega)\,d\omega\,dk\,dl. \quad (26)$$

Similarly, the spectral fluxes in frequency space $\Pi(\omega)$ are obtained by integrating over all wavenumbers and over a semi-infinite range of frequencies,

$$\Pi_{\mathrm{KE},1}(\Omega)=\int\int\int_{\omega\geq\Omega}T_{\mathrm{KE},1}(k,l,\omega)\,d\omega\,dk\,dl, \quad (27)$$

$$\Pi_{\mathrm{KE},2}(\Omega)=\int\int\int_{\omega\geq\Omega}T_{\mathrm{KE},2}(k,l,\omega)\,d\omega\,dk\,dl, \quad (28)$$

$$\Pi_{\mathrm{APE}}(\Omega)=\int\int\int_{\omega\geq\Omega}T_{\mathrm{APE}}(k,l,\omega)\,d\omega\,dk\,dl, \quad (29)$$

$$\Pi_{\mathrm{forcing}}(\Omega)=\int\int\int_{\omega\geq\Omega}T_{\mathrm{forcing}}(k,l,\omega)\,d\omega\,dk\,dl, \quad \text{and} \quad (30)$$

$$\Pi_{\mathrm{friction}}(\Omega)=\int\int\int_{\omega\geq\Omega}T_{\mathrm{friction}}(k,l,\omega)\,d\omega\,dk\,dl. \quad (31)$$

Following the terminology of Scott and Arbic (2007), we will call the budget obtained by summing the spectral fluxes (22)–(26) or (27)–(31) the integral energy budget. Note that, because we are using the depth-averaged energy equation, there are no interlayer spectral fluxes or transfers. See Sheng and Hayashi (1990a,b) and references therein for the derivation of energy equations in the

frequency domain for realistic atmospheric models and atmospheric datasets.

For simplicity, in this paper, we examine either spectral fluxes $\Pi(k)$ in wavenumber space or $\Pi(\omega)$ in frequency space. In future work, we will consider fluxes in which partial integrations are performed over both frequency and wavenumber, via

$$\Pi(K,\Omega) = \int_{k^2+l^2\geq K^2} \iint_{\omega\geq\Omega} T(k,l,\omega)\, d\omega\, dk\, dl. \qquad (32)$$

In the next section, we will show integral potential enstrophy budgets as well as integral energy budgets. The potential enstrophy budget is obtained through multiplication of (13) and (14) by $\delta\hat{q}_1^*/(1+\delta)$ and $\hat{q}_2^*/(1+\delta)$, respectively, followed by addition, taking the real parts, and integration.

e. *Energy and enstrophy budget of idealized model in frequency space*

The integral energy budget in wavenumber space of the nominal $F_L = 0.4$ QG simulation was examined in detail in Scott and Arbic (2007) and is discussed briefly here (Fig. 4a). The forcing term (magenta curve) is positive, indicating an energy gain over all wavenumbers. The bottom friction term (blue curve) is a sink of energy over all wavenumbers. The flux $\Pi_{\mathrm{APE}}(k)$ of available potential energy (green curve) is positive, meaning that potential energy cascades toward larger wavenumbers (smaller length scales; Salmon 1980). The black and red curves represent spectral fluxes $\Pi_{\mathrm{KE},1}(k)$ and $\Pi_{\mathrm{KE},2}(k)$ of upper- and lower-layer kinetic energy, respectively, with the latter being much smaller in magnitude. The negative values of these curves indicate an inverse cascade of energy toward lower wavenumbers (larger length scales). The cyan curve is the residual of the terms above. It is close to zero over all wavenumbers, indicating that the effects of the wavenumber filter in the energy budget of these runs are negligible, consistent with our results in Arbic and Flierl (2004).

The integral energy budget in frequency space is displayed in Fig. 4b. The terms behave similarly, with a positive forcing term (energy source), negative bottom friction term (energy sink), positive potential energy flux (forward cascade to small time scales), negative kinetic energy flux, and small residual. The negative spectral kinetic energy fluxes $\Pi_{\mathrm{KE},1}(\omega)$ and $\Pi_{\mathrm{KE},2}(\omega)$ indicate that an "inverse temporal cascade" exists alongside the well-known inverse cascade in space. An important difference between the budgets in frequency versus wavenumber space is that the fluxes in the frequency budget are "wider." The forward potential energy flux and inverse kinetic energy flux take on nonnegligible values immediately to the right of the low-frequency endpoints. In contrast, in wavenumber space these fluxes are close to zero over wide bands at the low end of the spectrum. Nonlinearities in the QG turbulence model apparently drive energy to the lowest frequencies allowed in the simulation, where these lowest frequencies are set by the simulation duration.

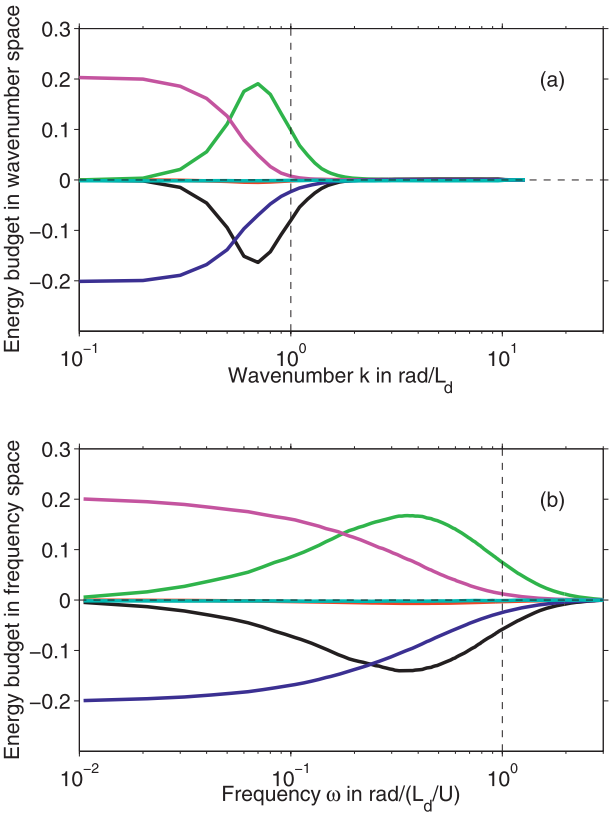

FIG. 4. Integral energy budgets of nominal two-layer $F_L = 0.4$ QG simulation in (a) wavenumber k space and (b) frequency ω space. Black and red curves denote spectral fluxes of upper- and lower-layer kinetic energy $\Pi_{\mathrm{KE},1}$ and $\Pi_{\mathrm{KE},2}$, respectively. Green curves denote spectral flux of APE Π_{APE}. Forcing is given by the magenta curve, whereas bottom Ekman friction is given by the blue curve. The cyan curve denotes the residual of the terms above. All terms nondimensionalized by $(\overline{u}_1 - \overline{u}_2)^3/L_d$.

The integral potential enstrophy budget is displayed in Fig. 5, in both the wavenumber and the frequency domains. Once again, forcing is denoted by the magenta curves and is positive, indicating a source of enstrophy. The bottom friction terms (blue curves) represent a sink, but one that is much less substantial than in the energy budgets. The flux of potential enstrophy by nonlinear terms (black and red curves for the upper and lower layers, respectively) is positive, indicating a forward flux of potential enstrophy down to small spatial scales (where enstrophy dissipation takes place) and small time scales.

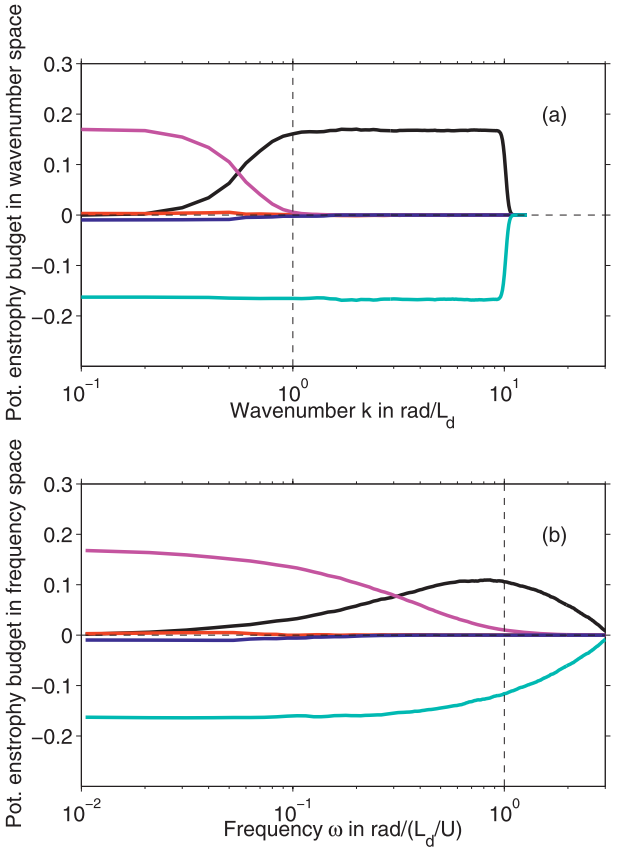

FIG. 5. Integral potential enstrophy budgets of nominal two-layer $F_L = 0.4$ QG simulation in (a) wavenumber k space and (b) frequency ω space. Black and red curves denote spectral fluxes of upper- and lower-layer potential enstrophy, respectively. Forcing is given by the magenta curve, whereas bottom Ekman friction is given by the blue curve. The cyan curve denotes the residual of the terms above and is assumed to be dominated by the dissipation of enstrophy by the wavenumber filter in the model. All terms nondimensionalized by $(\overline{u}_1 - \overline{u}_2)^2/L_d^3$.

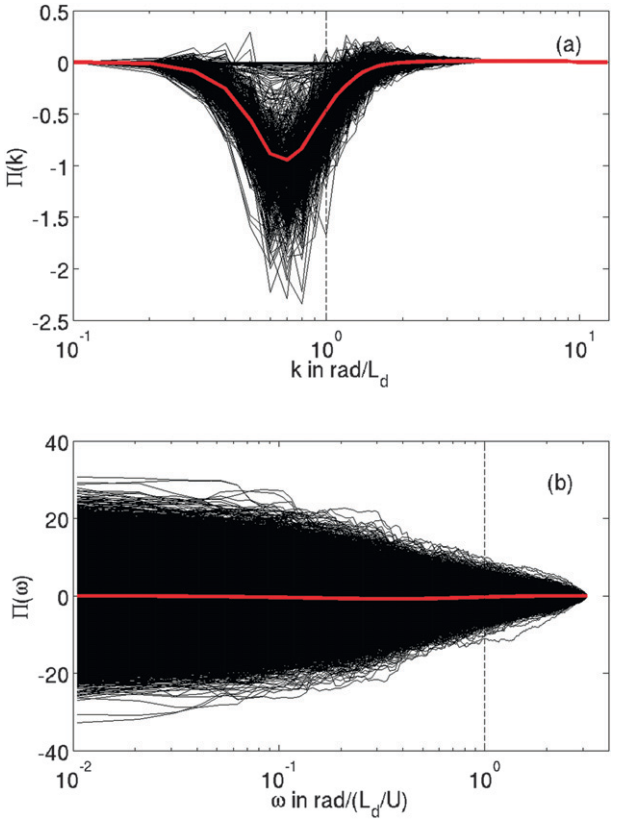

FIG. 6. Variability in individual realizations of spectral fluxes of upper-layer kinetic energy $\Pi_{KE,1}(k)$ and $\Pi_{KE,1}(\omega)$ computed from nominal two-layer $F_L = 0.4$ QG simulation. (a) Black curves are $\Pi_{KE,1}(k)$ computed from each of 600 individual snapshots in time, and the red curve is $\Pi_{KE,1}(k)$ computed from averaging over the 600 individual snapshots. (b) Black curves are $\Pi_{KE,1}(\omega)$ computed from each of 256^2 individual grid points, and the red curve is $\Pi_{KE,1}(\omega)$ computed from averaging over the 256^2 grid points. All terms nondimensionalized by $(\overline{u}_1 - \overline{u}_2)^3/L_d$.

The cyan curve again denotes the imbalance of the other terms. Here, the imbalance is much more substantial than in the energy budget. We assume that the imbalance is dominated by small-scale dissipation (the wavenumber filter), which is much more important in enstrophy budgets than in energy budgets. As in Fig. 4, we see in Fig. 5 that the fluxes in frequency space are wider, with a more rounded appearance than they have in wavenumber space.

f. Necessity for averaging over many grid points

It is necessary to average over many grid points to obtain an estimate of the spectral flux in frequency space. This point is illustrated in Figs. 6 and 7. Figure 6a shows the upper-layer spectral kinetic energy flux in wavenumber space $\Pi_{KE,1}(k)$, computed from each of the 600 "realizations" [individual snapshots (black curves)] of the nominal $F_L = 0.4$ QG solution. Averaging over the snapshots (red curve) is equivalent to integrating over all frequencies, which was done in Fig. 4a. Figure 6b displays the $\Pi_{KE,1}(\omega)$ plots computed at the 256^2 individual grid points in the QG model (black curves), alongside the $\Pi_{KE,1}(\omega)$ values computed after averaging over all of these grid points (red curve; equivalent to integrating over all wavenumbers, as in Fig. 4b). The range seen in $\Pi_{KE,1}(\omega)$ estimates at individual grid points is about 25 times larger than the range seen in $\Pi_{KE,1}(k)$ estimates in individual snapshots. The range in $\Pi_{KE,1}(\omega)$ values is especially large for low frequencies.

In Figs. 7a,b, we show the spectral fluxes $\Pi_{KE,1}(k)$ and $\Pi_{KE,1}(\omega)$, respectively, along with envelopes representing the variability seen in Fig. 6. The envelopes are computed as standard deviations of the individual realizations shown in Fig. 6, divided by the square root of

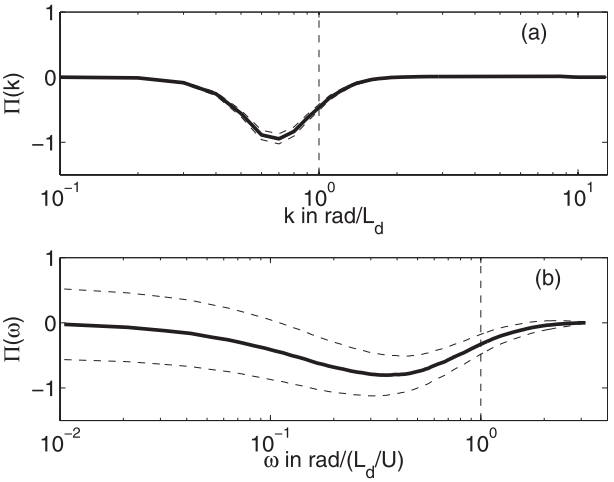

FIG. 7. (a) Upper-layer spectral kinetic energy flux $\Pi_{KE,1}(k)$ (solid curve) computed from nominal two-layer $F_L = 0.4$ QG simulation, shown along with envelopes representing variability of individual realizations of $\Pi_{KE,1}(k)$. See text for more description. (b) As in (a), but for $\Pi_{KE,1}(\omega)$. All terms nondimensionalized by $(\overline{u}_1 - \overline{u}_2)^3/L_d$.

the estimated number of degrees of freedom. The number of degrees of freedom for the $\Pi_{KE,1}(k)$ calculation is estimated by dividing the simulation duration by the correlation time scale. Similarly, the number of degrees of freedom for the $\Pi_{KE,1}(\omega)$ calculation is estimated by dividing the number of grid points (256^2) by the square of the correlation length scale. Consistent with the Fig. 6 results, the $\Pi_{KE,1}(k)$ envelopes are much smaller than the $\Pi_{KE,1}(\omega)$ envelopes.

g. *Effects of simulation duration and sampling frequency*

In this subsection, we examine the impact of the duration of the model simulations on the estimation of spectra, spectral fluxes, and spectral transfers in frequency space. We are motivated in part by the large envelopes computed in the previous subsection, which suggest a large uncertainty in the estimation of $\Pi_{KE,1}(\omega)$. If the uncertainty is indeed large, then different simulations of the nominal $F_L = 0.4$ QG run should yield substantially different estimates of $\Pi_{KE,1}(\omega)$. We can test this with simulations having different durations. We will examine spectral transfers, which identify sources and sinks of energy. We are interested in whether spectral transfers will identify nonlinear cascades as a source of low-frequency energy and whether this determination will change as lower frequencies become available in simulations with longer durations.

An examination of a nominal $F_L = 0.4$ simulation that is saved more frequently than the runs discussed thus far will shed light on some other issues of interest. We anticipate a sensitivity to sampling frequency in the spectra at high frequencies based on the nature of small-scale dissipation. Dissipation operators such as the wavenumber filter we employ here act preferentially on high wavenumbers and thus yield steep slopes at the high end of wavenumber spectra plots (Figs. 2a,c). The wavenumber filter does not act directly on small time scales, and therefore it is not clear that we will see similarly steep slopes at high frequencies. To confidently estimate the slopes at high frequencies, we need simulations that are sampled more frequently. Another motivation for examining slopes at high frequencies was noted earlier. At high frequencies, a slope steeper than -2 is required for the first moment of the frequency spectrum ω_E to be a meaningful quantity.

The frequency spectra of upper-layer kinetic energy in three simulations of the nominal $F_L = 0.4$ two-layer QG solution, with each having a different duration and sampling frequency, are displayed in Fig. 8a. The red curve is from the same simulation as the red curves in Fig. 2: 600 snapshots, each spaced one unit of nondimensional time $L_d/(\overline{u}_1 - \overline{u}_2)$ apart. The black curve is also sampled one unit of nondimensional time apart but is from a simulation that is 9 times as long (5400 snapshots). The blue curve is from a simulation that contains 2400 snapshots, each spaced 0.1 units of nondimensional time apart; it is more frequently sampled but shorter than the other two. The space- and time-averaged kinetic energies of the three simulations are equal to within 5%. Over the window of frequencies utilized in Fig. 2b, the slope of the blue curve (higher-frequency sampling) is -1.9, similar to the slope computed in that band for the red curve (-1.8). At higher frequencies, the slope of the blue curve is steeper than -2, as anticipated in discussions of the definition of ω_E. This steeper band is aliased into lower frequencies in the red and black curves (lower-frequency sampling) in Fig. 8a, as seen by the upturns at the high-frequency end of those curves.

The spectral fluxes of upper-layer kinetic energy in frequency space $\Pi_{KE,1}(\omega)$ are shown in Fig. 8b for the three simulations. Near nondimensional ω values on the order of one, the three curves agree very closely. At lower frequencies, the blue curve (short, rapidly sampled simulation) separates from the red and black curves by slight amounts. The red and black curves (longer simulations) stay close together over all the frequencies for which both are defined. The separation of the three curves is not nearly as large as the envelopes in Fig. 7b suggest they might be. For this reason we prefer the term ''envelopes'' in the discussion of Fig. 7b rather than error bars. In all three curves in Fig. 8b, the nonlinear kinetic energy flux extends out to the lowest frequencies, where the lowest

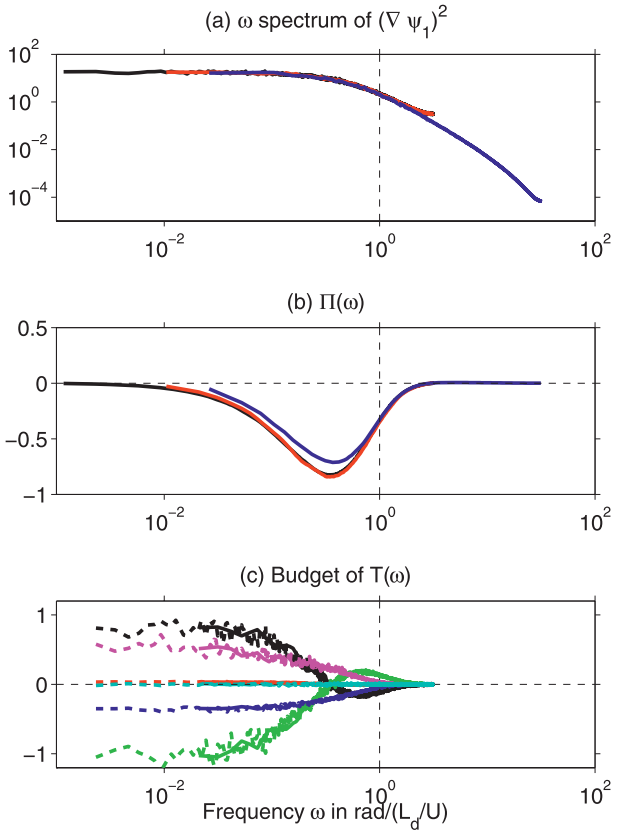

FIG. 8. (a) Frequency spectra and (b) spectral fluxes in frequency space $\Pi_{KE,1}(\omega)$ of upper-layer kinetic energy in three simulations of the nominal two-layer $F_L = 0.4$ QG solution. The red curve is as in Fig. 2, based on 600 snapshots spaced one unit of nondimensional time $L_d/(\overline{u}_1 - \overline{u}_2)$ apart. The blue curve is based on 2400 snapshots, spaced 0.1 units of nondimensional time apart. The black curve is based on 5400 snapshots, spaced one unit of nondimensional time apart. (c) Spectral transfers $T(\omega) = -\partial\Pi(\omega)/\partial\omega$, shown for the nominal 600-snapshot simulation (solid curves) and longer 5400-snapshot simulation (dashed curves). Colors in (c) represent different terms in the model energy budget as in Fig. 4.

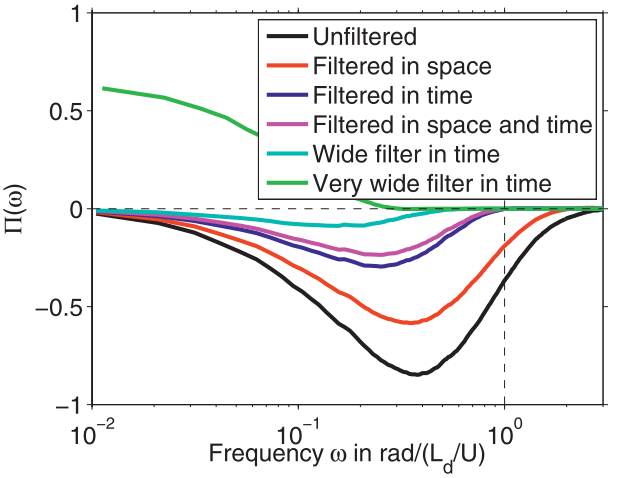

FIG. 9. Spectral flux $\Pi_{KE,1}(\omega)$ of upper-layer kinetic energy in frequency space computed from the 600-snapshot nominal two-layer $F_L = 0.4$ QG simulation (unfiltered) and from filtered versions of this simulation. The spatial filter is a Blackman filter that goes to zero at six grid points from the central grid point. The time filter is a Blackman filter that goes to zero at four units of nondimensional time $L_d/(\overline{u}_1 - \overline{u}_2)$ from the central time. The wide and very wide time filters are Blackman filters that go to zero at 9 and 17 units of nondimensional time from the central time, respectively. All terms nondimensionalized by $(\overline{u}_1 - \overline{u}_2)^3/L_d$.

frequency of any particular run is set by the duration of the run.

As discussed in many sources (e.g., Salmon 1978, 1980; Hua and Haidvogel 1986; Larichev and Held 1995; LaCasce 1996; among others), the transfer $T(k) = -[\partial\Pi(k)/\partial k]$ identifies wavenumbers that serve as energy sources and sinks. In like manner, $T(\omega) = -[\partial\Pi(\omega)/\partial\omega]$ can be used to identify energy sources and sinks as a function of frequency. Figure 8c shows the $T(\omega)$ budget for the 600-snapshot $F_L = 0.4$ QG simulation (solid curves), next to the budget for the longer-duration 5400-snapshot simulation (dashed curves). Different terms in the budget are denoted by the same colors as in Fig. 4. At low frequencies, the main balance is between the upper-layer kinetic energy flux $T_{KE,1}(\omega)$ and the potential energy flux $T_{APE}(\omega)$, with substantial contributions from forcing and friction. In the longer run, the various terms in the budget extend from their values at higher frequencies (which are close to the values seen in the shorter run) out to lower frequencies in a relatively flat manner. Figure 8c demonstrates that nonlinear cascades play a dominant role in maintaining variance out to frequencies as low as one-thousandth of the nondimensional frequency $(\overline{u}_1 - \overline{u}_2)/L_d$. We have not yet found a lower bound on the frequencies to which the QG turbulence model will push into. Considering that this model contains only eddies, which are normally described as having time scales of a year or less, and has no gyres, boundary currents, or other features that are normally associated with interannual and decadal time scales, this result is somewhat surprising.

Given that the kinetic energy flux dominates the low-frequency behavior, it is of interest to determine how large it is relative to the total energy in the system. The absolute value of the minimum (trough) of the flux $\Pi_{KE,1}(\omega)$, divided by the domain-integrated upper-layer kinetic energy in the simulation, is 0.09, in units of $(\overline{u}_1 - \overline{u}_2)/L_d$. Taking typical midocean values of 1–10 cm s^{-1} for $\overline{u}_1 - \overline{u}_2$ and 50 km for L_d, this amounts to 2×10^{-8} to 2×10^{-7} s^{-1}, in dimensional terms. Later we will compare this range to values computed from realistic models and from altimeter data.

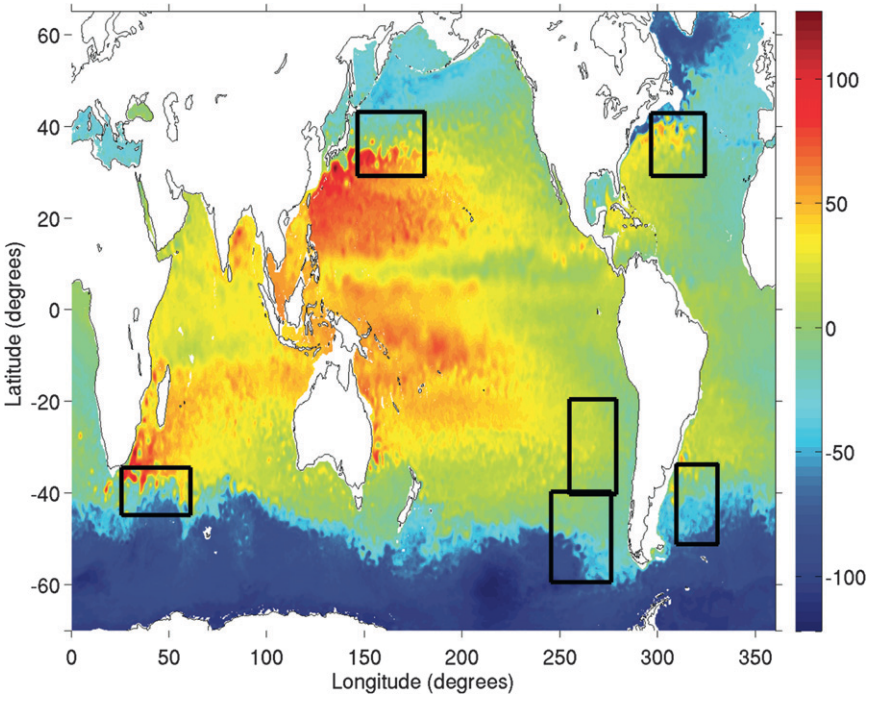

FIG. 10. Six subdomains used to compute spectra and spectral fluxes in 1/32° NLOM output, highlighted against the 15 Feb 2002 snapshot of sea surface height (cm) in the model: midlatitude southeast Pacific, high-latitude southeast Pacific, Agulhas, Malvinas, Gulf Stream, and Kuroshio.

h. Impact of spatial and temporal filtering on spectral fluxes in frequency space

In Fig. 9, motivated by the spatial and temporal filtering inherent in the creation of gridded satellite altimeter data, we show $\Pi_{KE,1}(\omega)$ computed from the nominal $F_L = 0.4$ QG simulation and from filtered versions of this simulation. Note that the filtering is performed on the model output after the model has been run, not during the run. The time filter is a Blackman filter that goes to zero at four units of nondimensional time $L_d/(\overline{u}_1 - \overline{u}_2)$ from the central time. The spatial filter goes to zero at six grid points from the central grid point, meaning it has a "full width at half maximum" (width at the half-power point) of 3.4 grid points or a wavelength of 0.83 L_d. Filtering in space or in time diminishes the negative lobe of the spectral flux substantially. Filtering in both space and time further diminishes the negative lobe. Widening the time filter distorts the spectral flux even more (cyan curve), to the point where it can eventually change sign (green curve). We will revisit this point later in the paper.

3. Results from the realistic ocean model

We use three full years of output (2001–03) from the nonassimilative version of the Naval Research Laboratory (NRL) Layered Ocean Model (NLOM). Data-assimilative versions of NLOM are in current use as a U.S. Navy operational model. NLOM is based on the primitive equation model of Hurlburt and Thompson (1980), but with greatly expanded capability (Wallcraft et al. 2003). It has six dynamical layers and a bulk mixed layer. Shriver et al. (2007) and references therein describe the NLOM grid, wind forcing, and other model details. The horizontal resolution of the NLOM simulation analyzed here is 1/32° in latitude and 45/1024° in longitude, on a model grid extending from 72°S to 65°N. For simplicity, we refer to the simulations as having 1/32° resolution. The simulation we used was saved at 6-h intervals over the 3 yr analyzed here.

Figure 10 displays a snapshot of sea surface height in NLOM. Six subdomains (regions) of interest, in which we will compute spectra and spectral fluxes, are shown. Four of the subdomains are in regions of intense boundary current and mesoscale eddy activity: the Kuroshio in the western North Pacific, the Gulf Stream in the western North Atlantic, the Agulhas off the southern tip of Africa, and the Malvinas in the western South Atlantic. Two additional subdomains are analyzed in the eastern South Pacific: a quiescent region in midlatitudes and a high-latitude region that touches upon the Antarctic Circumpolar Current in its southernmost portions.

In the subdomains in a realistic model (or observational oceanic dataset), spectral flux computations will be affected by energy fluxes into and out of the subdomains. Scott and Wang (2005) investigated the importance of subdomain size in the computation of spectral fluxes $\Pi_{KE,1}(k)$ in wavenumber space. They computed fluxes for subdomains 10°, 20°, and 40° on a side. The 10° subdomains yielded noisy results, "most likely indicating the importance of boundary terms relative to interior terms." However, their Fig. 2 shows that even the noisy results in the 10° × 10° subdomains are not qualitatively different from 20° × 20° results centered on the same point, which in turn are similar to the 40° × 40° results. Our subdomains in this paper contain roughly as many grid points as the 20° × 20° boxes in their paper. Therefore, our spectral fluxes should not be qualitatively affected by the size of our subdomains.

The NLOM computations are the most demanding calculations shown in this paper. Three years of 6-hourly global 1/32° NLOM sea surface heights represents 660 GB of output to sort through. Once extracted, the six subdomains constitute about 35 GB of output, which must be analyzed in both the time and space domains several times over to compute $\Pi_{KE,1}(\omega)$ and $\Pi_{KE,1}(k)$. For simplicity, we compute only $\Pi_{KE,1}$ in the NLOM integral energy budget and omit other terms. Also for simplicity, the factor $\delta/(1+\delta)$ is omitted from the computation of $\Pi_{KE,1}$, because stratification is not uniform across the extent of the model. Finally, the envelopes discussed in section 2f are omitted here because they would be very expensive to compute.

The procedure for analyzing NLOM output is as follows: The NLOM sea surface heights are first low-pass filtered in time to remove motions with periods of 3 days or less. This is done because such high-frequency motions cannot be geostrophic. Next, we compute surface streamfunctions $\psi_1 = g\eta/f$, where η is sea surface height; $g = 9.8$ m s^{-2} is the gravitational acceleration; and f is the Coriolis parameter, which varies as the sine of the model gridpoint latitude (Vallis 2006). Then, for each of the six subdomains shown in Fig. 10, each snapshot of ψ_1 is detrended in space with a two-dimensional least squares fit. Following this, the ψ_1 field is tapered in space with a two-dimensional function constructed of nine overlapping Hanning windows in each spatial direction, with each window having a width one-fifth of the domain extent in that direction. Tapering is also done on each time series at each model grid point, using the same window as in the QG calculation (nine overlapping Hanning windows). This type of detrending and tapering is standard in computations of Fourier transforms of nonperiodic data. Fourier transforms are then repeatedly utilized to compute derivatives. For simplicity, we base the increment lengths of the wavenumbers in the east–west direction on the length of the increments at the central latitude of the box. Thus, we do not account for the convergence of meridians in our spectral calculations.

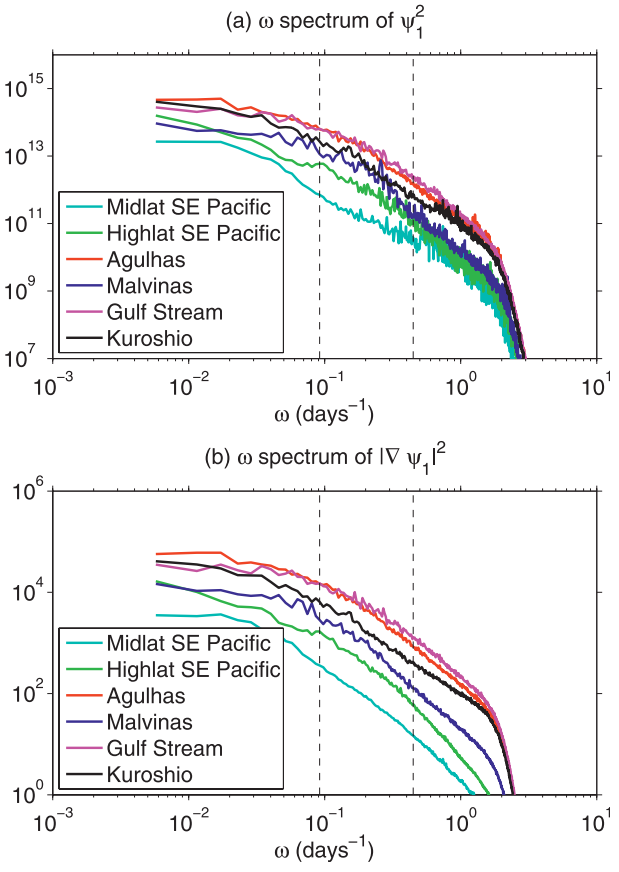

FIG. 11. Frequency spectra of the variance of (a) surface ocean streamfunction $\psi_1 = g\eta/f$, where g is gravitational acceleration, f is the Coriolis parameter, and η is sea surface height drawn from NLOM output in subdomains shown in Fig. 10, and (b) geostrophic velocities computed from this streamfunction. Dashed lines are drawn at the frequencies corresponding to periods of 14 and 68.4 days.

The frequency spectra of the variance of the NLOM streamfunction ψ_1 in the six subdomains are displayed in Fig. 11a. Figure 11b displays the frequency spectra of the variance of geostrophic velocities (kinetic energy; $|\nabla\psi_1|^2$). As in the QG results, the NLOM frequency spectra display a "flatness" at the lowest frequencies and a steeper slope at higher frequencies, in what might be called the "mesoscale band."[3] The dashed vertical

[3] Schmitz (1996) (see also references therein, including Schmitz and Luyten 1991) defines the mesoscale band as 20–200 days. This band contains most of the kinetic energy in regions of strong boundary currents.

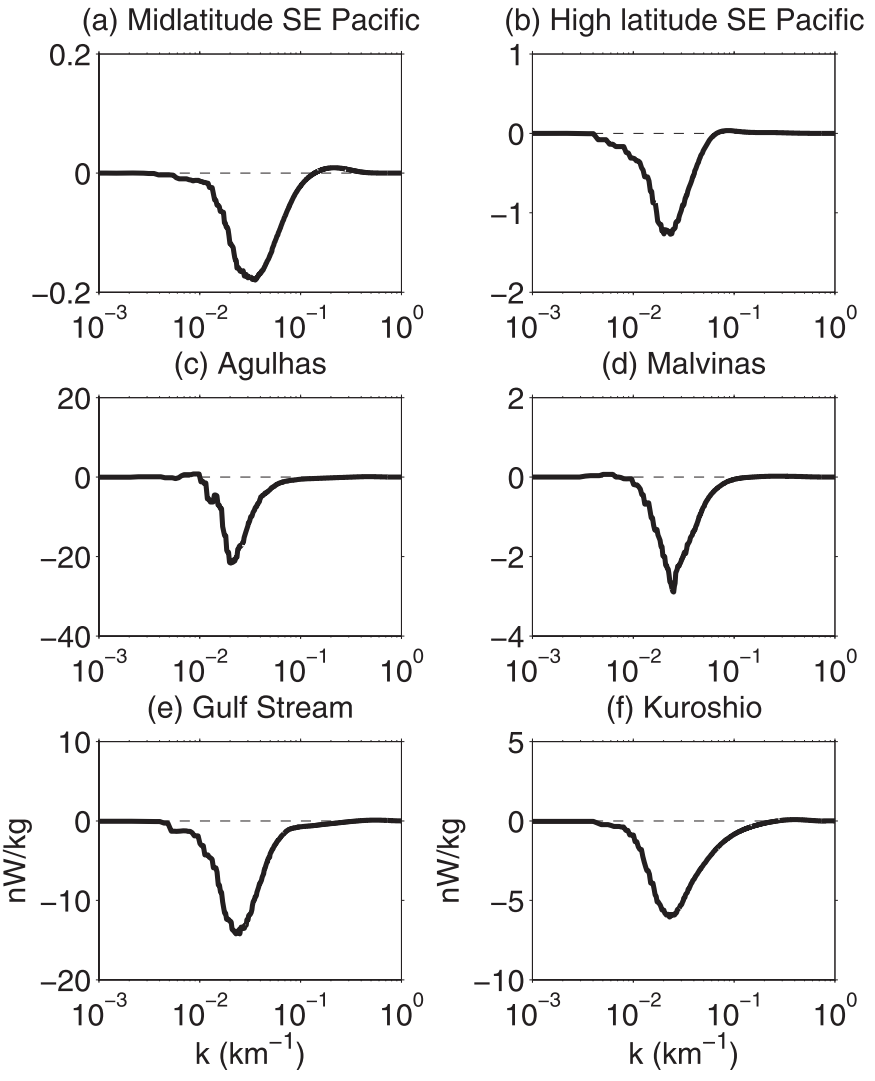

FIG. 12. Spectral fluxes of surface ocean geostrophic kinetic energy $\Pi_{KE,1}(k)$ in wavenumber space computed from NLOM output in subdomains shown in Fig. 10.

lines in Fig. 11 are at frequencies corresponding to periods of 68.4 and 14 days, respectively. In the next section, we will discuss the slopes in this band along with slopes computed in the same band from satellite altimeter data. This band was chosen because it lies in the mesoscale band, is resolved by both the NLOM and AVISO results utilized in this paper, appears to lie in approximately the same part of parameter space in which the band analyzed in Figs. 2b,d lies (i.e., in the steep part of the QG spectrum), and covers a range of frequencies equal to the range of the band analyzed in Figs. 2b,d. The highest frequencies in the NLOM spectra show a steep dropoff due to the 3-day low-pass filter we employed.

Figure 12 displays the spectral fluxes $\Pi_{KE,1}(k)$ in wavenumber space computed from the six subdomains in NLOM. As in previous studies (Scott and Wang 2005; Scott and Arbic 2007; Schlösser and Eden 2007; Tulloch et al. 2011), the negative lobes representing inverse cascades are ubiquitous (seen in every subplot). As noted in Scott and Wang (2005), the magnitude of the spectral fluxes varies by two orders of magnitude across ocean basins.

Figure 13 displays the spectral fluxes $\Pi_{KE,1}(\omega)$ in frequency space (shown as thick solid curves) computed from the six subdomains in NLOM. The fluxes are dominated by negative lobes, implying that nonlinear terms drive a cascade of kinetic energy toward longer time scales. Comparison of the subplots in Fig. 13 to the subplots in Fig. 12 demonstrates that the magnitudes of the spectral fluxes $\Pi_{KE,1}(\omega)$ in the various subdomains are comparable to but smaller than the magnitudes of the corresponding spectral fluxes $\Pi_{KE,1}(k)$. The ratio of the

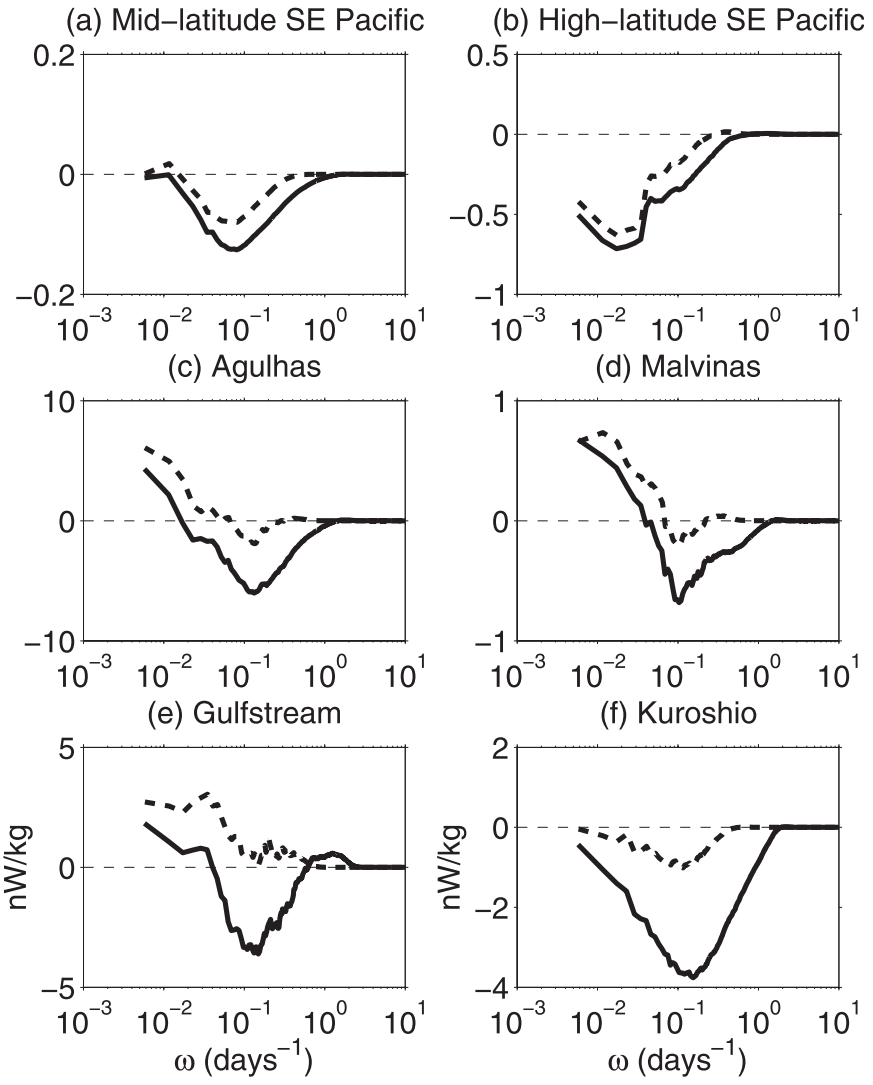

FIG. 13. Thick solid curves are spectral fluxes of surface ocean geostrophic kinetic energy $\Pi_{KE,1}(\omega)$ in frequency space computed from NLOM output in subdomains shown in Fig. 10. Thick dashed curves represent fluxes computed after the NLOM output has been temporally filtered. See text for details.

minimum (trough) of the flux $\Pi_{KE,1}(\omega)$ to the domain-averaged kinetic energy lies in the range from 5.8×10^{-8} to 1.4×10^{-7} s^{-1}, similar to the range estimated from the QG results in section 2g. This suggests to us that, as in the QG simulations, nonlinearities play an important role in the maintenance of low-frequency energy in NLOM.

The dashed thick curves in Fig. 13 are spectral fluxes $\Pi_{KE,1}(\omega)$ computed from NLOM output that has been temporally smoothed, in an attempt to mimic the filtering inherent in the gridded satellite altimeter data. As in the calculations made from filtered QG model output, the filtering is performed on NLOM output after the model has been run, not during the runs. For NLOM we use a Blackman filter, which goes to zero at 7 days from the central time. The 7-day width is chosen to match the 7-day output frequency of the AVISO data. As in the QG results, temporal smoothing diminishes the inverse temporal cascade, to the point where in some cases (see especially Fig. 13e) the flux changes sign.

4. Results from satellite altimeter data

We use 840 snapshots of the two-satellite AVISO 1/3° Mercator grid ''reference'' product (Le Traon et al. 1998; Ducet et al. 2000), beginning with 14 October 1992 and ending with 12 November 2008. The AVISO record we utilize is much longer than the NLOM record (16 versus 3 yr), but has a much lower temporal sampling

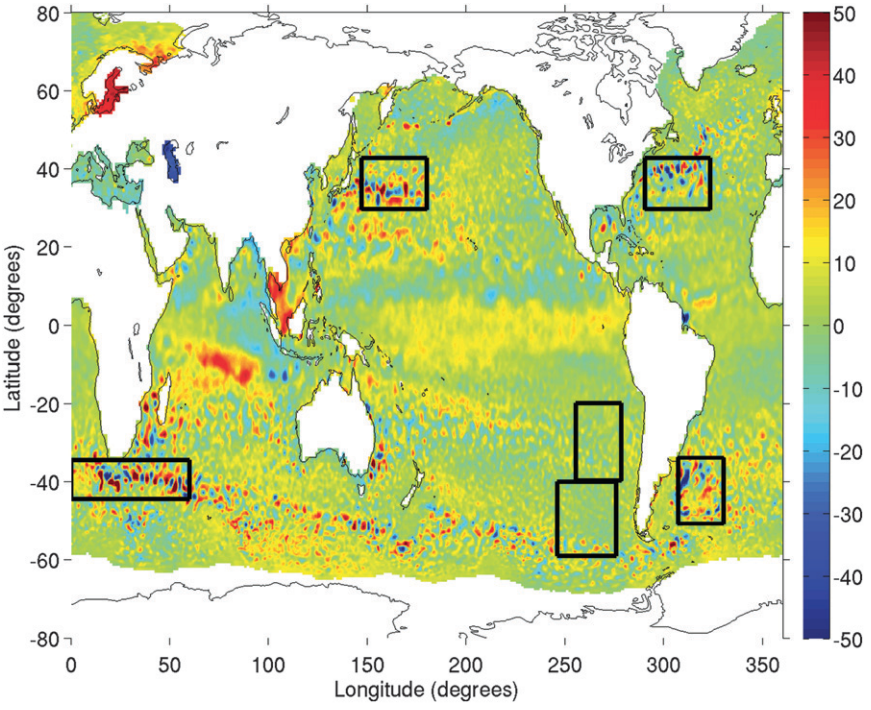

FIG. 14. Six subdomains used to compute spectra and spectral fluxes in 1/3° AVISO gridded satellite altimeter data, highlighted against the 27 Dec 2006 snapshot of sea surface height anomaly (cm) in AVISO: midlatitude southeast Pacific, high-latitude southeast Pacific, Agulhas, Malvinas, Gulf Stream, and Kuroshio.

rate (7 days versus 6 h). The spatial resolution is also much lower (1/3° versus 1/32°). The analysis procedure used on the AVISO data is very similar to that used on the NLOM output, with the main exception being that we do not subject the AVISO data to the 3-day low-pass filtering.

Figure 14 displays the six subdomains over which we compute spectra and spectral fluxes from AVISO data. The subdomains correspond closely to those utilized in the NLOM analysis. The correspondence is not exact because of the lack of points in shallow waters in NLOM (see Shriver et al. 2007, and references therein). The misfit between the boundaries of the NLOM and altimeter subdomains is largest in the Agulhas subdomain. As in the NLOM computation, we compute only $\Pi_{KE,1}$ from AVISO, omitting other terms in the integral energy budget, and we omit the stratification factor $\delta/(1 + \delta)$.

Figure 15 displays the frequency spectra of the variance of ψ_1 and of surface geostrophic velocity computed from AVISO. As in the NLOM and idealized QG results, the AVISO spectra are flat at the lowest frequencies and show a steeper slope at higher frequencies.

Table 1 presents the slopes of the frequency spectra in NLOM and AVISO, over the period band 14–68.4 days, for the six subdomains and for both streamfunction and velocity variance. A few general conclusions can be noted. For the most part, the NLOM spectral slopes hover around the −1.8 and −2.6 values found in the high-frequency QG model results, albeit with wide variability (deviations vary by as much as 0.4 in either direction). A notable exception is the slope of the streamfunction variance in the midlatitude southeast Pacific, which is actually less steep than the slope of the velocity variance (at higher frequencies, the streamfunction variance in this subdomain is steeper than the velocity variance, as is more typically the case). Consistent with the highly smoothed nature of the AVISO product, the AVISO slopes are steeper than the NLOM slopes, often substantially so (deviations vary by as much as 2.0). With the exception of the midlatitude southeast Pacific patch noted above, the difference between slopes in NLOM streamfunction variance and NLOM velocity variance spectra, or in AVISO streamfunction variance and AVISO velocity variance spectra, ranges from −0.3 to −0.7. These differences are remarkably consistent between AVISO and NLOM output computed for the same subdomain, despite the fact that the AVISO slopes are generally much steeper than the NLOM slopes.

The values of the slopes depend, of course, on the band chosen for computing the least squares fit. The slopes of

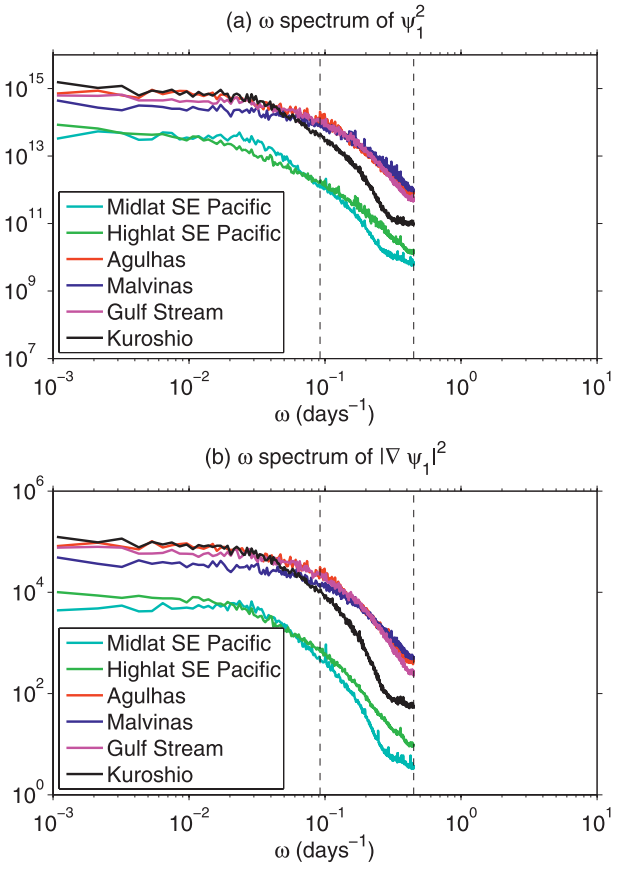

FIG. 15. Frequency spectra of the variance of (a) surface ocean streamfunction $\psi_1 = g\eta/f$, where g is gravitational acceleration, f is the Coriolis parameter, and η is sea surface height drawn from gridded $^1/_3°$ AVISO data in subdomains shown in Fig. 14, and (b) geostrophic velocities computed from this streamfunction. Dashed lines are drawn at the frequencies corresponding to periods of 14 and 68.4 days.

the AVISO spectra are not very clean in the 14–68.4-day band. Note, for instance, the upturns at the high-frequency end of the Kuroshio results in Fig. 15. This is likely due to aliasing; see the discussion of the upturns in Fig. 8a. We also computed spectral slopes over the 38–184-day band, which gets us away from the problems at the high-frequency end for AVISO. For the sake of brevity, the slopes over the 38–184-day band are not given here in detail, but we do note that over most of the six subdomains they are more consistent between NLOM and AVISO than the 14–68.4-day band results. This does not mean that the 38–184-day band is without problems. It is not as cleanly separated from the flat low-frequency part of the spectrum as the 14–68.4-day band is. Thus, the slopes in the 38–184-day band are more likely to represent a mixture of the dynamics of two distinct regimes. The 38–184-day band slopes are generally shallower than the 14–68.4-day band slopes.

Periods shorter than 14 days are not represented in the AVISO data, whereas periods longer than 1095 days are not represented in the 3-yr NLOM record used here. Slopes computed from NLOM output over a frequency band corresponding to periods between 3 and 14.6 days are considerably steeper than those in Table 1. For the 3–14.6-day band, the differences in slopes between NLOM streamfunction and velocity variance spectra range from −0.5 to −1.1, except in the high-latitude southeast Pacific patch, which yields a slope that is steeper in velocity variance by 0.2. For periods between 294 and 2940 days, the slopes of the AVISO frequency spectra range from −0.5 to −0.1 for streamfunction variance and from −0.2 to 0.1 for velocity variance, with the streamfunction variance always being steeper, by amounts ranging from −0.02 to −0.3. These values lie near the low-frequency QG values reported earlier of −0.4 and −0.1 for streamfunction and velocity variance and −0.2 difference between these.

All six of the AVISO subdomains display a tendency for the low-frequency variance of zonal velocity to be larger than that of meridional velocity. Figure 16 plots the frequency spectra of zonal and meridional velocity variance in the midlatitude southeast Pacific, in which this tendency is most extreme. The zonal velocity variance integrated over periods of 420–5880 days is 2.3 times larger than the meridional velocity variance. In the

TABLE 1. The first column is the six subdomains of World Ocean examined in both NLOM output and AVISO gridded satellite altimeter data. The second through fifth columns are the slopes of frequency spectra of variance of surface streamfunction ψ_1 and variance of surface geostrophic velocity (kinetic energy; $|\nabla\psi_1|^2$). Slopes are computed as least squares fits over the frequency band corresponding to periods of 14–68.4 days (see dashed vertical lines in Figs. 11, 15). The sixth column is NLOM Δ, the slope in the NLOM streamfunction variance spectrum minus the slope in the NLOM velocity variance spectrum. The seventh column is as in the sixth column, but for AVISO.

Subdomain	NLOM ψ_1^2	AVISO ψ_1^2	NLOM $\lvert\nabla\psi_1\rvert^2$	AVISO $\lvert\nabla\psi_1\rvert^2$	NLOM Δ	AVISO Δ
Midlatitude southeast Pacific	−1.8	−3.7	−2.0	−3.5	0.2	−0.2
High-latitude southeast Pacific	−2.4	−3.3	−2.1	−3.0	−0.3	−0.3
Agulhas	−2.5	−3.4	−1.9	−2.8	−0.7	−0.7
Malvinas	−2.9	−3.1	−2.2	−2.3	−0.7	−0.7
Gulf Stream	−2.2	−3.8	−1.6	−3.2	−0.6	−0.6
Kuroshio	−2.6	−4.4	−1.9	−3.8	−0.7	−0.6

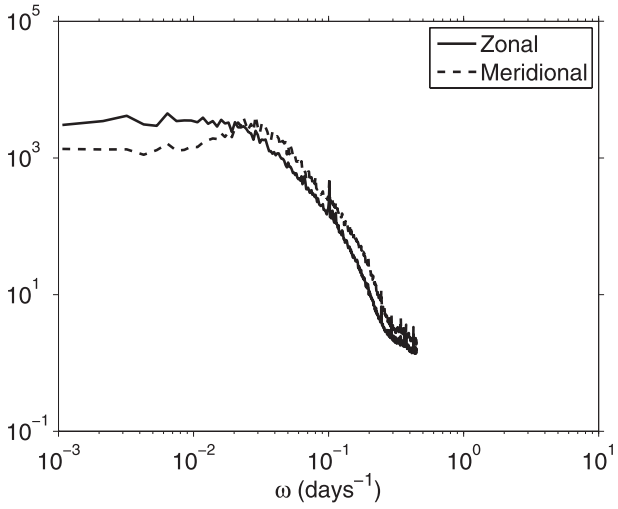

FIG. 16. Frequency spectra of the variance of zonal and meridional geostrophic velocity, computed from AVISO gridded altimeter data in the midlatitude southeast Pacific patch shown in Fig. 14.

other five subdomains, the zonal velocity variance integrated over these periods ranges from 1.1 to 1.6 times larger than the meridional variance. This tendency for zonal velocity variance to exceed meridional velocity variance at low frequencies was noted by Richman et al. (1977), from analysis of a current-meter record much shorter than the present-day AVISO record.

Figure 17 displays the spectral fluxes $\Pi_{KE,1}(k)$ in wavenumber space over the six subdomains of AVISO data. As in the QG and NLOM computations, the dominant feature is a negative lobe, representing an inverse cascade toward larger length scales. Also as in the NLOM computations, the magnitudes of the spectral fluxes vary by two orders of magnitude over ocean basins. Envelopes were computed assuming a 35-day correlation time over the 16-yr record, and are small enough that they are difficult to see in Fig. 17.

Figure 18 displays the spectral fluxes $\Pi_{KE,1}(\omega)$ in frequency space over the six subdomains of AVISO data. To test the sensitivity to windowing, fluxes are computed in three different ways. The baseline calculations (black curves) use the full time interval of 840 snapshots, tapered with nine overlapping Hanning windows each 168 snapshots wide. We also subdivided the time series into time intervals of 160 days each with 9 different overlapping realizations (blue curves) and into time intervals of 80 days each with 19 different overlapping realizations (red curves). At higher frequencies, the three methods yield similar results, suggesting that our computation technique is relatively robust. Some subdomains (high-latitude southeast Pacific, Agulhas, and arguably the Malvinas) display a negative lobe indicating an inverse temporal cascade, consistent with the QG and NLOM results. However, the Gulf Stream, Kuroshio, and mid-latitude southeast Pacific display a predominantly forward cascade (positive spectral flux) in frequency space. This may be due to interesting physics in some regions of the ocean that are not captured well in either NLOM or the QG turbulence model. The smoothing exercises in previous sections suggest an alternative possibility, that forward temporal cascades could be artifacts of the filtering inherent in the creation of gridded satellite altimeter data products. For the subdomains with a clear negative spectral flux (Agulhas and high-latitude southeast Pacific), the ratios of the minimum (trough) negative flux $\Pi_{KE,1}(\omega)$ to the kinetic energy are 6.0 and 4.0×10^{-8} s^{-1}, respectively, consistent with the QG and NLOM results (see discussions in earlier sections) and suggestive of the importance of nonlinearities in maintaining energy at low frequencies.

5. Summary and discussion

Motivated by the ubiquity of time series in oceanic data, the relative lack of studies of geostrophic turbulence in the frequency domain, and the interest in quantifying the contributions of intrinsic oceanic nonlinearities to oceanic frequency spectra, we have undertaken a comprehensive examination of spectra and spectral fluxes of surface oceanic geostrophic flows in the frequency domain. We have shown that the frequency spectra of the streamfunction (sea surface height) variance and geostrophic velocity variance (kinetic energy) in idealized flat-bottom f-plane two-layer QG turbulence models, realistic ocean general circulation models, and gridded satellite altimeter data exhibit qualitative similarities, with steeper slopes at higher frequencies and flatter slopes at lower frequencies. In the data and models considered here, the flat slopes at lower frequencies continue out to the lowest frequencies allowed by the duration of the record.

We demonstrate here that the machinery of geostrophic turbulence, which is usually discussed in the wavenumber domain, is useful in the frequency domain as well. Through examination of the energy budgets of the QG model in frequency space, we find that the quantity $\Pi_{KE,1}(\omega)$, the spectral flux of upper-layer kinetic energy in the frequency domain, documents an energy cascade toward longer time scales driven by the action of nonlinearities, much like $\Pi_{KE,1}(k)$, the spectral flux of upper-layer kinetic energy in the wavenumber domain, documents an inverse cascade of energy toward larger length scales. The $\Pi_{KE,1}(\omega)$ is "wider" than $\Pi_{KE,1}(k)$, consistent with the action of nonlinearities at the longest time scales permitted by the record duration. A budget of the spectral transfers $T(\omega) = -\partial\Pi(\omega)/\partial\omega$

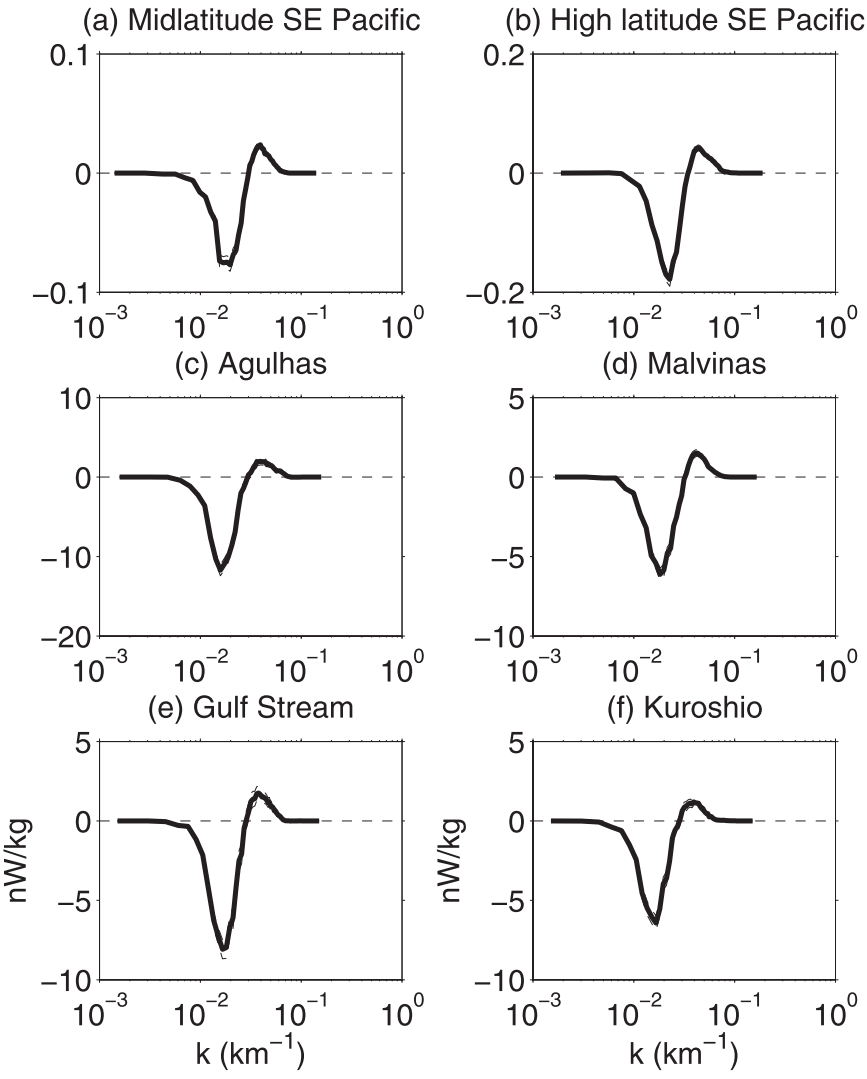

FIG. 17. Spectral fluxes $\Pi_{KE,1}(k)$ in wavenumber space (thick curves) computed from gridded 1/3° AVISO data in subdomains shown in Fig. 14. Envelopes are drawn with dashed curves.

further demonstrates the importance of nonlinearities in maintaining low-frequency energy in the QG turbulence model examined here.

We have also calculated spectral fluxes in frequency space from NLOM, a realistic near-global ocean general circulation model, and from the AVISO gridded satellite altimeter dataset. The $\Pi_{KE,1}(\omega)$ values computed from the realistic model also document a nonlinear cascade of kinetic energy toward longer time scales. The $\Pi_{KE,1}(\omega)$ values computed from AVISO gridded satellite altimeter data yield more ambiguous results. Some subdomains (regions) are dominated by an ''inverse temporal cascade,'' whereas others exhibit a forward temporal cascade. Computations done with temporally and/or spatially smoothed QG model output, as well as temporally smoothed NLOM output, demonstrate that the spectral flux computations are highly susceptible to the smoothing inherent in the construction of gridded altimeter products. It remains to be seen whether the forward temporal cascades seen in some subdomains in altimeter data represent real physics not present in the models analyzed here or artifacts of the smoothed nature of gridded altimeter data.

A comprehensive comparison of the slopes of frequency spectra in the QG turbulence model, the realistic NLOM simulation, and AVISO altimetry data is given in this paper. In the QG model, the slope of the velocity variance spectra at the high-frequency end is −1.8, close to the −2 prediction from dimensional considerations of a kinetic energy cascade in frequency space (Tennekes

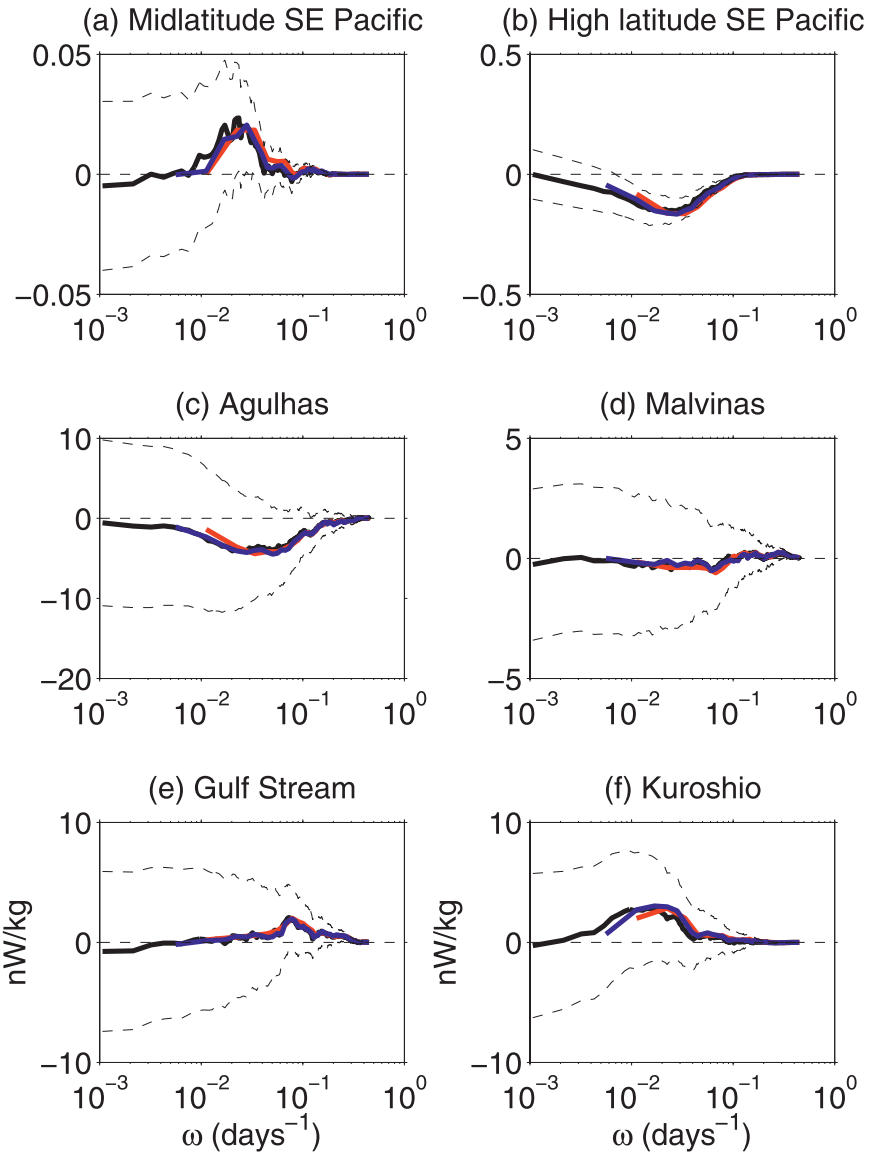

FIG. 18. Spectral fluxes $\Pi_{KE,1}(\omega)$ in frequency space (thick curves) computed from gridded 1/3° AVISO data in subdomains shown in Fig. 14. Thick black curves denote baseline results computed over 840 weekly snapshots. Thick blue (red) curves denote results computed over overlapping intervals of 160 (80) weekly snapshots each. Dashed curves denote envelopes of thick black curves.

and Lumley 1972). The slopes in frequency spectra of streamfunction and velocity variance do not differ by −2, as they do in wavenumber spectra, which represents a quantitative failure of the Taylor (1938) hypothesis relating frequency to wavenumber spectra. In the band of higher frequencies analyzed in the QG model, the slopes differ by −0.8. In the band 14–68.4 days, the differences in the slopes of the streamfunction and velocity variance spectra vary between −0.3 and −0.7 in NLOM and AVISO, in five of the six subdomains analyzed. There is some consistency between slopes in the idealized QG model and the realistic model (NLOM), but the latter shows wide variability from one region to another. In the 14–68.4-day band, the slopes in the AVISO dataset are significantly steeper, consistent with the highly filtered nature of that product. The failure of the Taylor (1938) hypothesis in our results is reminiscent of discussions in Hayashi and Golder (1977), who found no simple relationship between kinetic energy spectra in the frequency and wavenumber domains in their space–time

analysis of realistic atmospheric models and atmospheric datasets.

The time scales in two-layer QG turbulence exhibit a sensitivity to the strength of linear bottom Ekman friction, somewhat similar to the sensitivity previously documented in the length scales. Although there are some interesting differences discussed in section 2c, an important similarity is that the time scales in two-layer QG turbulence tend to be longer than the imposed nondimensional time $L_d/(\overline{u_1} - \overline{u_2})$, just as the length scales tend to be larger than the imposed length scale L_d.

We end by briefly discussing natural extensions of this work. In this study, we have looked only at the spectra and spectral fluxes of geostrophic flows. In future work, we will consider spectra and spectral fluxes computed from the full velocity field in realistic models that contain ageostrophic flows. In this study, we have looked only at spectra and spectral fluxes in wavenumber space or in frequency space, but never in mixed frequency–wavenumber space. In section 2d, we developed the theory for the more general flux $\Pi(k, \omega)$. We anticipate that examination of spectra in mixed wavenumber–frequency space may help to illuminate some of the limitations of Taylor's (1938) hypothesis. We anticipate that examination of mixed fluxes $\Pi(k, \omega)$, in flows that include ageostrophic motions such as near-inertial waves and tides as well as geostrophic eddies, could yield insights into interactions between these different classes of motions. Motivated by the results in Fig. 8c, we also anticipate that the spectral transfers $T(\omega)$ could be useful diagnostics of the role of nonlinearity in maintaining low-frequency variability in the climate system. In ocean models, $T(\omega)$ could be computed for both the atmospheric forcing and the oceanic nonlinearities, potentially helping to determine how much low-frequency variability in the ocean is driven by atmospheric forcing (e.g., Griffies and Tziperman 1995) and how much is due to intrinsic oceanic nonlinearities (e.g., Penduff et al. 2011).

Acknowledgments. The authors thank two anonymous reviewers for their helpful comments, which led to substantial improvements to this manuscript. Helpful discussions with Ru Chen, Charlie Doering, Nicolas Ducousso, Steve Griffies, Thierry Penduff, and Carl Wunsch are gratefully acknowledged. BKA and AJM were supported by Office of Naval Research Grant N00014-11-1-0487, National Science Foundation (NSF) Grant OCE-09607820, and University of Michigan faculty startup funds. RBS acknowledges support from NSF Grants OCE-0960834 and OCE-0851457; a contract with the National Oceanography Centre, Southampton; and a NASA subcontract to Boston University. GRF received support from NSF Grant OCE-0960826. JFS and JGR were supported by the projects ''Global and remote littoral forcing in global ocean models'' and ''Ageostrophic vorticity dynamics of the ocean,'' respectively, both sponsored by the Office of Naval Research under program element 601153N. The NRL contribution has been approved for public release.

REFERENCES

Arbic, B. K., and G. R. Flierl, 2003: Coherent vortices and kinetic energy ribbons in asymptotic, quasi two-dimensional f-plane turbulence. *Phys. Fluids,* **15,** 2177–2189.

——, and ——, 2004: Baroclinically unstable geostrophic turbulence in the limits of strong and weak bottom Ekman friction: Application to midocean eddies. *J. Phys. Oceanogr.,* **34,** 2257–2273.

——, and R. B. Scott, 2008: On quadratic bottom drag, geostrophic turbulence, and oceanic mesoscale eddies. *J. Phys. Oceanogr.,* **38,** 84–103.

——, G. R. Flierl, and R. B. Scott, 2007: Cascade inequalities for forced–dissipated geostrophic turbulence. *J. Phys. Oceanogr.,* **37,** 1470–1487.

Canuto, C., M. Y. Hussaini, A. Quarteroni, and T. A. Zang, 1988: *Spectral Methods in Fluid Mechanics*. Springer-Verlag, 567 pp.

Chelton, D. B., J. C. Ries, B. J. Haines, L.-L. Fu, and P. S. Callahan, 2001: Satellite altimetry. *Satellite Altimetry and Earth Sciences,* L.-L. Fu and A. Cazenave, Eds., Academic Press, 1–131.

——, M. G. Schlax, and R. M. Samelson, 2011: Global observations of nonlinear mesoscale eddies. *Prog. Oceanogr.,* **91,** 167–216.

Ducet, N., P.-Y. Le Traon, and G. Reverdin, 2000: Global high-resolution mapping of ocean circulation from TOPEX/Poseidon and ERS-1 and -2. *J. Geophys. Res.,* **105,** 19 477–19 498.

Efimov, V. B., A. N. Ganshin, G. V. Kolmakov, P. V. E. McClintock, and L. P. Mezhov-Deglin, 2009: Acoustic turbulence in superfluid ^{4}He. *J. Low Temp. Phys.,* **156,** 95–115, doi:10.1007/s10909-009-9894-y.

——, ——, ——, ——, and ——, 2010: Rogue waves in superfluid helium. *Eur. Phys. J. Spec. Top.,* **185,** 181–193, doi:10.1140/epjst/e2010-01248-5.

Ferrari, R., and C. Wunsch, 2010: The distribution of eddy kinetic and potential energies in the global ocean. *Tellus,* **62A,** 92–108, doi:10.1111/j.1600-0870.2009.00432.x.

Flierl, G. R., 1978: Models of vertical structure and the calibration of two-layer models. *Dyn. Atmos. Oceans,* **2,** 341–381.

Fu, L.-L., and G. R. Flierl, 1980: Nonlinear energy and enstrophy transfers in a realistically stratified ocean. *Dyn. Atmos. Oceans,* **4,** 219–246.

Ganshin, A. N., V. B. Efimov, G. V. Kolmakov, L. P. Mezhov-Deglin, and P. V. E. McClintock, 2008: Observation of an inverse energy cascade in developed acoustic turbulence in superfluid helium. *Phys. Rev. Lett.,* **101,** 065303, doi:10.1103/PhysRevLett.101.065303.

Griffies, S. M., and E. Tziperman, 1995: A linear thermohaline oscillator driven by stochastic atmospheric forcing. *J. Climate,* **8,** 2440–2453.

Hasselmann, K., 1976: Stochastic climate models. Part I. Theory. *Tellus,* **28,** 473–485.

Hayashi, Y., 1982: Space-time spectral analysis and its applications to atmospheric waves. *J. Meteor. Soc. Japan,* **60,** 156–171.

——, and D. G. Golder, 1977: Space-time spectral analysis of mid-latitude disturbances appearing in a GFDL general circulation model. *J. Atmos. Sci.,* **34,** 237–262.

Hua, B. L., and D. B. Haidvogel, 1986: Numerical simulations of the vertical structure of quasi-geostrophic turbulence. *J. Atmos. Sci.,* **43,** 2923–2936.

Hughes, C. W., and S. D. P. Williams, 2010: The color of sea level: Importance of spatial variations in spectral shape for assessing the significance of trends. *J. Geophys. Res.,* **115,** C10048, doi:10.1029/2010JC006102.

Hurlburt, H. E., and J. D. Thompson, 1980: A numerical study of Loop Current intrusions and eddy shedding. *J. Phys. Oceanogr.,* **10,** 1611–1651.

LaCasce, J. H., 1996: Baroclinic vortices over a sloping bottom. Ph.D. dissertation, Massachusetts Institute of Technology-Woods Hole Oceanographic Institution Joint Program, 220 pp.

Larichev, V., and G. Reznik, 1976a: Strongly nonlinear two-dimensional isolated Rossby waves. *Oceanologia,* **16,** 547–550.

——, and ——, 1976b: Two-dimensional Rossby soliton: An exact solution. *Rep. USSR Acad. Sci.,* **231,** 1077–1079.

——, and I. M. Held, 1995: Eddy amplitudes and fluxes in a homogeneous model of fully developed baroclinic instability. *J. Phys. Oceanogr.,* **25,** 2285–2297.

Le Traon, P.-Y., F. Nadal, and N. Ducet, 1998: An improved mapping method of multisatellite altimeter data. *J. Atmos. Oceanic Technol.,* **15,** 522–534.

——, P. Klein, and B.-L. Hua, 2008: Do altimeter wavenumber spectra agree with the interior or surface quasigeostrophic theory? *J. Phys. Oceanogr.,* **38,** 1137–1142.

McWilliams, J. C., 1984: The emergence of isolated coherent vortices in turbulent flow. *J. Fluid Mech.,* **146,** 21–43.

Pedlosky, J., 1987: *Geophysical Fluid Dynamics*. 2nd ed. Springer-Verlag, 710 pp.

Penduff, T., M. Juza, B. Barnier, J. Zika, W. K. Dewar, A.-M. Treguier, J.-M. Molines, and N. Audiffren, 2011: Sea level expression of intrinsic and forced ocean variabilities at interannual time scales. *J. Climate,* **24,** 5652–5670.

Richman, J. G., C. Wunsch, and N. G. Hogg, 1977: Space and time scales of mesoscale motion in the western North Atlantic. *Rev. Geophys. Space Phys.,* **15,** 385–420.

Riviere, P., A. M. Treguier, and P. Klein, 2004: Effects of bottom friction on nonlinear equilibration of an oceanic baroclinic jet. *J. Phys. Oceanogr.,* **34,** 416–432.

Salmon, R., 1978: Two-layer quasi-geostrophic turbulence in a simple special case. *Geophys. Astrophys. Fluid Dyn.,* **10,** 25–52.

——, 1980: Baroclinic instability and geostrophic turbulence. *Geophys. Astrophys. Fluid Dyn.,* **15,** 167–211.

Schlösser, F., and C. Eden, 2007: Diagnosing the energy cascade in a model of the North Atlantic. *Geophys. Res. Lett.,* **34,** L02604, doi:10.1029/2006GL027813.

Schmitz, W. J., Jr., 1996: On the world ocean circulation: Volume I: Some global features/North Atlantic circulation. Woods Hole Oceanographic Institution Tech. Rep. WHOI-96-03, 148 pp.

——, and J. R. Luyten, 1991: Spectral time scales for mid-latitude eddies. *J. Mar. Res.,* **49,** 75–107.

Scott, R. B., and F. Wang, 2005: Direct evidence of an oceanic inverse kinetic energy cascade from satellite altimetry. *J. Phys. Oceanogr.,* **35,** 1650–1666.

——, and B. K. Arbic, 2007: Spectral energy fluxes in geostrophic turbulence: Implications for ocean energetics. *J. Phys. Oceanogr.,* **37,** 673–688.

Sheng, J., and Y. Hayashi, 1990a: Observed and simulated energy cycles in the frequency domain. *J. Atmos. Sci.,* **47,** 1243–1254.

——, and ——, 1990b: Estimation of atmospheric energetics in the frequency domain during the FGGE year. *J. Atmos. Sci.,* **47,** 1255–1268.

Shriver, J. F., H. E. Hurlburt, O. M. Smedstad, A. J. Wallcraft, and R. C. Rhodes, 2007: 1/32° real-time global ocean prediction and value-added over 1/16° resolution. *J. Mar. Syst.,* **65,** 3–26.

Stern, M. E., 1975: Minimal properties of planetary eddies. *J. Mar. Res.,* **33,** 1–13.

Taylor, G. I., 1938: The spectrum of turbulence. *Proc. Roy. Soc. London,* **164,** 476–490.

Tennekes, H., and J. L. Lumley, 1972: *A First Course in Turbulence*. MIT Press, 300 pp.

Thompson, A. F., and W. R. Young, 2006: Scaling baroclinic eddy fluxes: Vortices and energy balance. *J. Phys. Oceanogr.,* **36,** 720–738.

——, and ——, 2007: Two-layer baroclinic eddy heat fluxes: Zonal flows and energy balance. *J. Atmos. Sci.,* **64,** 3214–3231.

Tulloch, R., J. Marshall, C. Hill, and K. S. Smith, 2011: Scales, growth rates, and spectral fluxes of baroclinic instability in the ocean. *J. Phys. Oceanogr.,* **41,** 1057–1076.

Vallis, G. K., 2006: *Atmospheric and Oceanic Fluid Dynamics: Fundamentals and Large-Scale Circulation*. Cambridge University Press, 745 pp.

Wallcraft, A. J., A. B. Kara, H. E. Hurlburt, and P. A. Rochford, 2003: The NRL Layered Global Ocean Model (NLOM) with an embedded mixed layer submodel: Formulation and tuning. *J. Atmos. Oceanic Technol.,* **20,** 1601–1615.

Wunsch, C., 2009: The oceanic variability spectrum and transport trends. *Atmos.–Ocean,* **47,** 281–291.

——, 2010: Toward a midlatitude ocean frequency–wavenumber spectral density and trend determination. *J. Phys. Oceanogr.,* **40,** 2264–2281.

Xu, Y., and L.-L. Fu, 2011: Global variability of the wavenumber spectrum of oceanic mesoscale turbulence. *J. Phys. Oceanogr.,* **41,** 802–809.